Pergamon

Journal of Structural Geology, Vol. 18, Nos 2/3, pp. 321 to 340, 1996

0191-8141/96 $15.00+0.00

0191-8141(95)00091-7

Faulting-related displacement gradients and strain adjacent to the Awatere strike-slip fault in New Zealand

TIMOTHY A. LITTLE

Geology Department, Victoria University of Wellington, P.O. Box 600, Wellington, New Zealand

(*Received* 7 *January* 1994; *accepted in revised form* 12 *July* 1995)

Abstract—Three hundred and ten faults, most with slips of < 2 m, were observed along 3 km of seacliffs near an active dextral-reverse fault. The density of post-early Pliocene faults increases with proximity to this major fault. Most faults are oblique-normal. Younger dextral-reverse faults have larger displacements and are concentrated in a ~300 m wide zone bordering the active fault. Distribution of fault attitudes and slip-vector pitches is apparently similar for faults of both sets across a range of slip dimensions (from cm to tens of metres). Fault displacement vs cumulative frequency in this linear sample are related by a power-law exponent of 0.78 over the cm–m range in slip, indicating that the largest faults are the chief contributors to bulk strain.

Displacement gradients are locally homogeneous and increase toward the Awatere fault from very small to very large approaching the trace. A new algebraic technique is used to measure faulting-related strains in these rocks. Strains are prolate (reflecting transtension) except adjacent to the Awatere fault where they are oblate (transpression). Faulting-related strains do not compare with geodetic strain rates except near the main fault, suggesting that most faults are relict, and that ongoing transpressive deformation is elastically released during coseismic slip along the main fault. The relict faults formed in a divergent zone between two rotating blocks. Displacement across this zone was 40–50° relative to strike. The data suggest that this angle is approximately the critical angle at which normal faults will initiate rather than strike-slip faults in such zones.

INTRODUCTION

Little is known about the nature and extent of distributed faulting in the blocks between major crustal faults. Is the relationship between the displacement and frequency of faults in major fault zones fractal (Marrett & Allmendinger 1990, 1991, Scholz & Cowie 1990)? With increasing distance from a large fault, in what way and at what rate does subsidiary faulting result in the accumulation of displacement and strain? What might such relationships tell us about processes of fault growth and maturation (Wojtal & Mitra 1986, Cowie & Scholz 1992)? Many computer techniques have been devised to invert fault-slip data for a best-fit solution for the deviatoric stress tensor. In addition to requiring assumptions that reduce their usefulness (Wojtal & Pershing 1991, Pollard *et al.* 1993), they exclude from consideration two important types of field observations: (1) the magnitude of offset or displacement on a fault; (2) the spatial relationship of faults to each other.

After describing the tectonic context of the Awatere fault and the characteristics of subsidiary faulting developed near that structure, I outline a simple algebraic technique for finite strain analysis of fault sets that is a modification of Wojtal's (1986, 1989) method. This technique is applied to fault-slip data collected in well-exposed Pliocene rocks near the active Awatere fault in New Zealand. Estimates of permanent brittle strain obtained from this technique are compared with those using the moment tensor summation technique (Marrett & Allmendinger 1990, Peacock & Sanderson 1993), and with a century's worth of accumulated geodetic strain for the same region. The results of this study provide insight into: (1) a new method for kinematic analysis of natural fault sets; (2) the structural character of regional geodetic strain in areas of active tectonic deformation; (3) kinematic controls on faulting style and role of fault-block tilting in zones of oblique divergence; and (4) temporal and spatial variation in the character of distributed faulting adjacent to a major strike-slip fault.

TECTONICS OF THE MARLBOROUGH FAULTS

The Marlborough faults splay northeastward from the Alpine fault to form part of the actively deforming plate boundary zone between the Pacific and Australian plates on the South Island of New Zealand (Norris *et al.* 1990) (Figs. 1a & b). Near the coast in the northern part of the South Island, the faults cut a Cretaceous–Neogene sequence of marine sedimentary rocks on continental crust, and are underlain by a W-dipping slab of oceanic lithosphere of the Pacific plate at 100–200 km depth (Anderson *et al.* 1993). During the past 5 m.y., the Pacific plate has moved west-southwest relative to the Australian plate at a velocity of ~41 mm yr^{-1} (DeMets *et al.* 1990), resulting in dextral-reverse slip on the NE striking Marlborough faults (Lamb & Bibby 1989).

Geodetic strain and distribution of slip across the Marlborough faults

In the northeastern South Island, geodetic and earthquake focal mechanism data indicate that the direction of maximum horizontal shortening trends 110–115° across a wide region in Marlborough (Fig. 1b). Assum-

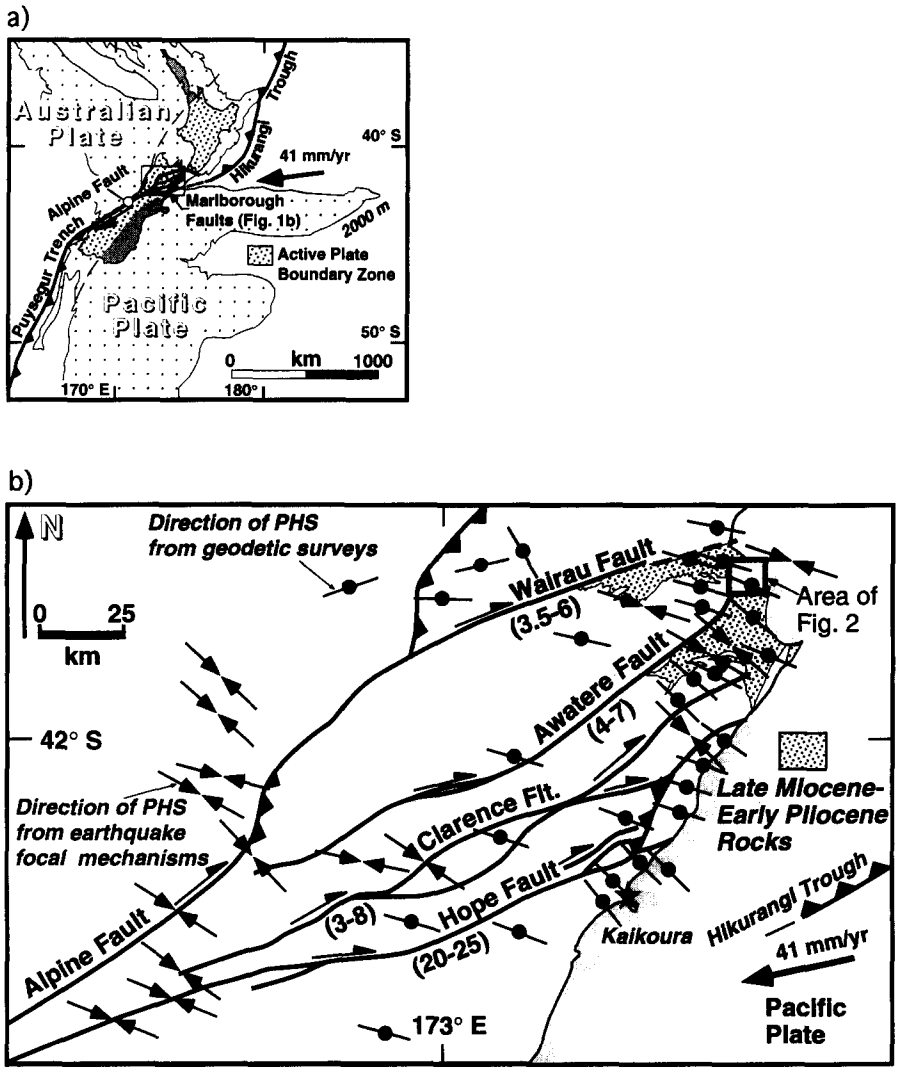

Fig. 1. (a) Simplified tectonic map of New Zealand showing relative motion of Pacific plate relative to Australian plate (from DeMets *et al.* 1990), the actively deforming plate boundary zone (stippled), the Alpine fault, and the Marlborough faults. (b) Tectonic map of the Marlborough faults, South Island, New Zealand. See Fig. 1(a) for location. Active fault traces and estimates of fault slip-rates (mm yr^{-1}, in parentheses) compiled from Van Dissen & Yeats (1991) and Kneupfer (1992). Direction of maximum incremental horizontal shortening (MHS) from geodetic surveys shown with ball-and-bar symbol and taken from Bibby (1976, 1981), Walcott (1984) and Lamb & Bibby (1989); MHS inferred from earthquake focal mechanism solutions (double arrows), from Arabasz & Robinson (1976) and Anderson *et al.* (1993). Local velocity of Pacific plate with respect to Australian plate calculated from Nuvel-1 pole of DeMets *et al.* (1990).

ing there are no velocity gradients parallel to the plate margin, and that deformation is uniformly distributed, this shortening azimuth is consistent with the DeMets *et al.* (1990) relative plate velocity for the Pacific–Australia plate boundary zone (see, for example, Walcott 1978). Bibby (1981) used the same assumption about the displacement field to integrate geodetic strain rates and show that the accumulation of geodetic strain across northeastern Marlborough during the past century can account for the total Pacific–Australia plate motion. Based on estimates of late Quaternary fault slip rates, Wellman (1983) suggested that 60% of the relative plate motion was accomplished by co-seismic slip on the Marlborough faults, with the remainder occurring by distributed deformation within the intervening blocks. According to this interpretation, 40% of the measured geodetic strain would represent permanent inelastic strain accumulating between major faults (see also Lamb 1988). A more recent compilation of late Quaternary fault slip rates suggests that the Marlborough faults can account for most of the plate motion (Kneupfer 1992). Slip on the Hope fault, alone, accomplishes half of the relative plate motion (Cowan 1990). Seismic moment summation of large historical earthquakes are consistent with co-seismic slip on major faults being the chief agent of plate motion (Pearson 1993). These results are hampered by large uncertainties associated with dating of offset terraces on the one hand, and the short duration of the seismic record on the other.

Shallow seismicity in Marlborough during the last three decades has been diffuse, and focal mechanisms of large ($Ms > 5.5$) events indicate transpression of crustal blocks between the major Marlborough faults, rather than slip along their boundaries (Anderson *et al.* 1993). On a larger time scale, Roberts (1992) describes palaeomagnetic evidence for 20–30° of clockwise rotation of parts of coastal Marlborough since the late Miocene.

Lamb (1988) and Lamb & Bibby (1989) noted a lack of evidence for internal deformation of major fault blocks in Marlborough and argue that distributed plate margin deformation occurs by complex rotations of these rigid blocks resting on the subducting slab. This paper is concerned with the nature and magnitude of distributed faulting deformation adjacent to one of the Marlborough faults, in an area where late Neogene faults are especially abundant and well exposed.

Awatere fault and White Bluffs exposure

Near the coast, mapping of Neogene–Quaternary features indicates that the active Awatere dextral-slip fault strikes 063, dips ~85° to the NW and has a reverse sense of throw (Fig. 2). Estimates of late Quaternary slip rates for the Awatere fault based on offset terraces are 4–7 mm yr^{-1} and indicate horizontal/vertical slip ratios of >10 (Kneupfer 1992). Near the coast, an inactive strand of the fault is concealed beneath unfaulted late Quaternary alluvium several km to the south of the presently active strand (Fig. 2). Stratigraphic and structural studies indicate that the Awatere fault (including the inactive strand) is <7 m.y. old and has a post-late Miocene net dextral-slip of >32 km, corresponding to mean slip rates of >5 mm yr^{-1} (Little 1994). The active coastal fault offsets the gently NE-dipping Miocene–Pliocene unconformity with ~2 km of dextral-strike separation, providing a maximum constraint for finite dextral-slip on that segment of the Awatere fault.

On the uplifted, northern side of the fault at the coast, folded Miocene–early Pliocene marine strata that dip 5–15° to the east or south are juxtaposed against Quaternary alluvium. The Neogene rocks are deformed by upright folds that have gentle interlimb angles (> 160°)

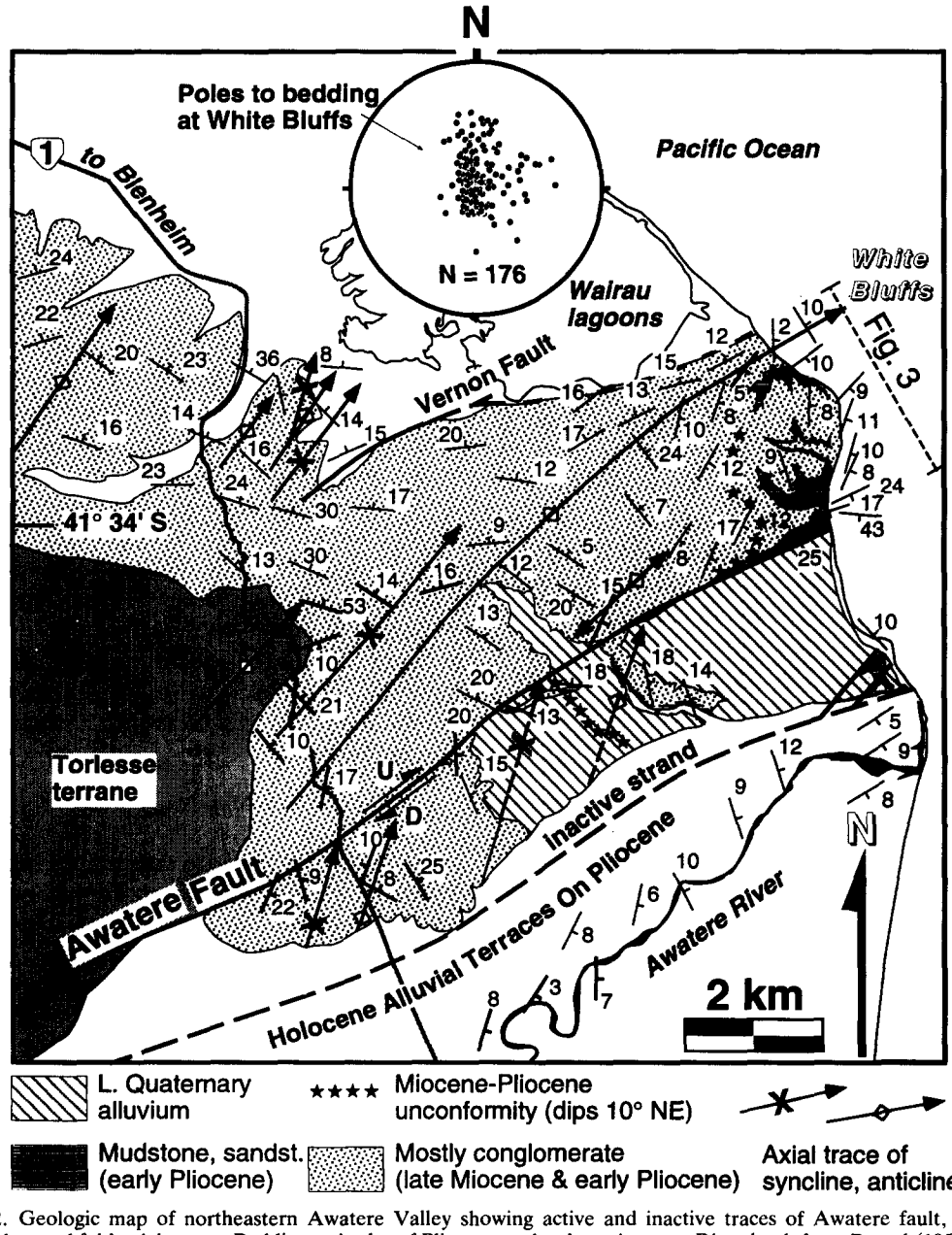

Fig. 2. Geologic map of northeastern Awatere Valley showing active and inactive traces of Awatere fault, bedding attitudes, and fold axial traces. Bedding attitudes of Pliocene rocks along Awatere River bank from Russel (1959). Inset lower hemisphere stereogram shows poles to bedding in faulted late Miocene–early Pliocene sequence at White Bluffs.

and rounded hinges trending ~33° anticlockwise from the local strike of the Awatere fault (Figs. 2 and 5e). Oblique tensile fractures on both sides of the Awatere fault near the coast indicate that the fault propagated upward through these rocks as a mode III dislocation with a process zone several km wide (Little in press).

FAULTING STYLES AND SLIP-KINEMATIC PATTERN

Fault sets and cross-cutting relationships

White Bluffs, over 260 m high, expose late Miocene–early Pliocene bedrock on the north side of the Awatere fault. A traverse ~3 km long crosses 310 faults in these coastal cliffs (Fig. 3). Two sets of faults were recognized on the basis of fault-kinematic style and cross-cutting relationships. The older set consists of oblique-normal faults, both sinistral and dextral, that generally dip moderately or steeply to the N, NW or NE. These occur in domino-style arrays throughout the cliffs (Fig. 4). Variable tilting of these faults about easterly strikes causes a corresponding scattering of bedding poles at White Bluffs (Fig. 2, inset). The other set consists chiefly of dextral-reverse faults that dip steeply to the NW or are sub-vertical (Fig. 4, locations 1–3). These locally cross-cut the older oblique-normal faults, and are only common within 300 m of the Awatere fault. Both sets of faults occur as: (1) 'cliff-scale' faults, with trace lengths of >1 m (these generally traverse the entire outcrop width or intersect other faults that do); and (2) 'pebble-scale' faults cutting conglomerate pebbles up to 30 cm in diameter. The latter generally terminate within a few cm of the edges of the pebble.

The slip-kinematics of faulting White Bluffs is remarkable for the similarity of its pattern across the spectrum of sampled fault sizes and fault position across the study region, and also for its departure from traditional models for subsidiary conjugate faulting in zones of strike-slip faulting (Tchalenko 1970, Hancock 1985). The mean fault strikes at 270, which is 27° clockwise from the Awatere fault (Fig. 5a). Most faults of all types dip to the north. The mean dip angle of cliff-scale faults in their present orientation is 65°, but increases to 70° if tilted 'domino-style' faults (the early set) are restored by rotation of local bedding back to horizontal (Fig. 5b). This distribution of fault attitudes is approximately the same for the pebble-scale faults (Fig. 5a). Faults of all sizes are dominantly oblique-slip. Overall, dextral faults outnumber sinistral faults 2:1 and normal-slip faults outnumber reverse-slip faults 3:1. Figure 6 is a graphical representation of the sampled kinematic spectrum of faults, based on dip angle, sense of dip-slip, sense of strike-slip, and slip-vector pitch (either measured or assigned, as discussed below). Note the abundance of oblique-normal faults, both dextral and sinistral, across a range of slip-vector pitches. Given the transpressional setting of the Awatere fault, this was an unexpected result. Dextral-reverse faults form a less abundant subset of the data. Overprinting relationships indicate that reverse-separation faults are younger than oblique-normal faults. Comparison of data for large (>1 m long) and small (pebble length) faults supports the conclusion that the fault kinematic pattern is essentially independent of scale (Fig. 6).

Slip-vector pattern of early oblique-normal faults

Across the spectrum of sampled range of fault sizes, slip-vector pitch and strike-slip sense varies systematically with fault strike. Early oblique-normal faults occur in all three zones and constitute 80% of the sample (Fig. 5c). These early faults have a mean strike of 272 but deviate on either side of this mean by as much as 40°. Most NE-striking faults are dextral; most SE-striking faults are sinistral. E–ESE-striking faults are approximately normal-dip-slip. The dominant sense of throw for all of these, down to the north, is opposite to that on the Awatere fault. The left-hand side of Fig. 7 shows variation of measured slip-vector pitches in the oblique-normal faults as a function of fault strike and includes data from all fault sizes. Note the down-dip slip lineation for E–ESE-striking faults, and a transition to sub-horizontal lineations, either dextral and sinistral, for faults on either side of the mean strike. The faulting pattern is not a conjugate one, but comprises a continuum of oblique-slip. Nearly pure dextral-slip faults strike sub-parallel to the Awatere fault (Fig. 7).

A computer inversion for the deviatoric stress tensor using the method of Gephart (1990) yielded a maximum principal compressive stress (σ_1) plunging 10° to 090, a sub-vertical intermediate stress (σ_2), and a least compressive stress (σ_3) plunging 16° to 183 (Little in press). The best-fit solution had a stress ratio, R, of 0.1, suggesting a prolate or constrictional state of stress in which σ_2 and σ_3 were nearly equal in magnitude. Using the algebraic technique of Ritz (1994), this deviatoric stress model was used to predict values of slip-vector pitch as a function of fault strike for the early oblique-normal fault set. The dashed lines on the left-hand side of Fig. 7 are the results contoured for differing values of fault dip. These data were used to assign slip-vector pitches to normal-separation faults on which a slip lineation could not be measured.

Slip-vector pattern of late dextral-reverse faults

Most of these faults are steeply NW-dipping or sub-vertical and developed after domino-style tilting of earlier oblique-normal faults, which they locally cross-cut (Fig. 4). The faults are chiefly dextral-reverse and are clustered near the Awatere fault. Throw on the late faults, chiefly up-to-the-north, is sympathetic with that on the Awatere fault. Of the 12 faults in the total sample at White Bluffs that have a displacement of > 10 m, 10 belong to this set.

Most late faults strike NE and dip steeply NW (Fig. 4). Some strike sub-parallel to the Awatere fault, but the dominant mode is 10–20° clockwise from that structure in an approximate 'Reidel shear' orientation (Fig. 5a, inset, & d). A subset of faults strike ~50–60° clockwise

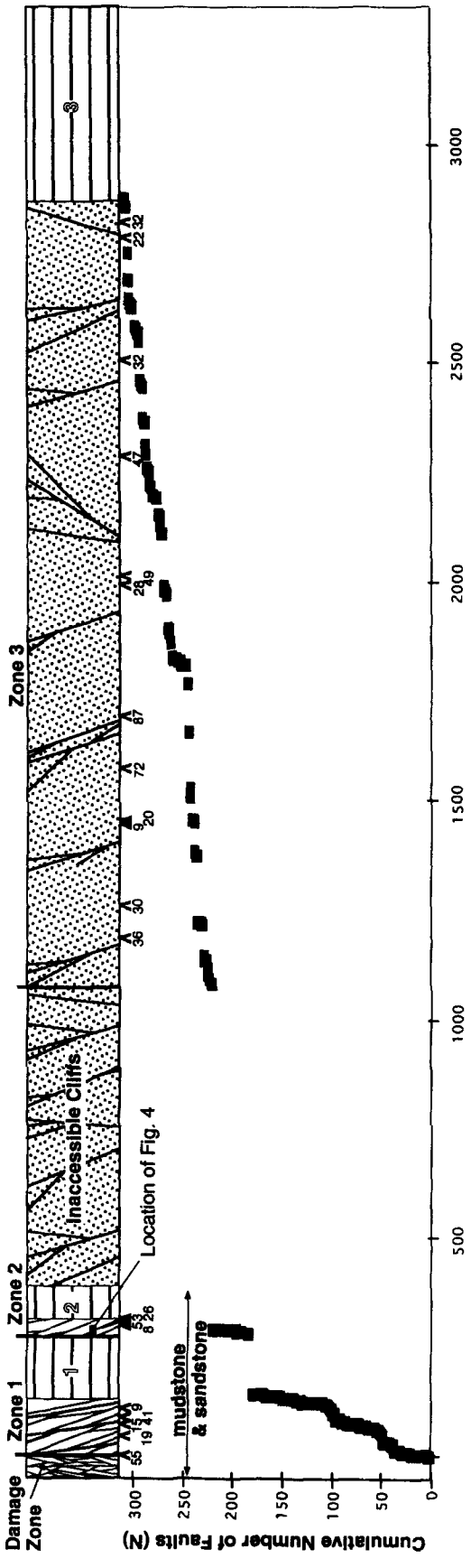

Fig. 3. Cumulative number of faults observed in profile plotted against distance normal to Awatere fault. Schematic profile shows Awatere fault, location of zones outlined in text, and position of covered intervals on the transect (amount of missing outcrop width specified in m). Horizontal line patterns represent total length of covered rock in each zone.

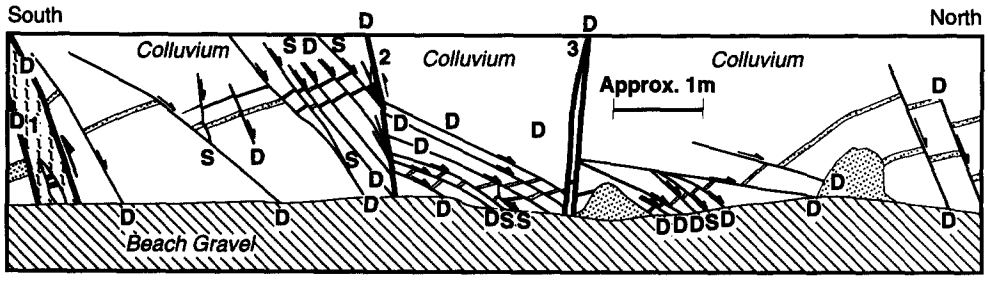

Fig. 4. Line drawing of fault array exposed in profile along cliff face in zone 2 (compiled from outcrop photomosaic). See Fig. 3 for approximate location. The letters S and D refer to oblique-slip faults, with a sinistral and dextral strike-slip component, respectively. Note how dextral-reverse faults (Nos 1, 2 and 3) cross-cut older oblique-normal faults.

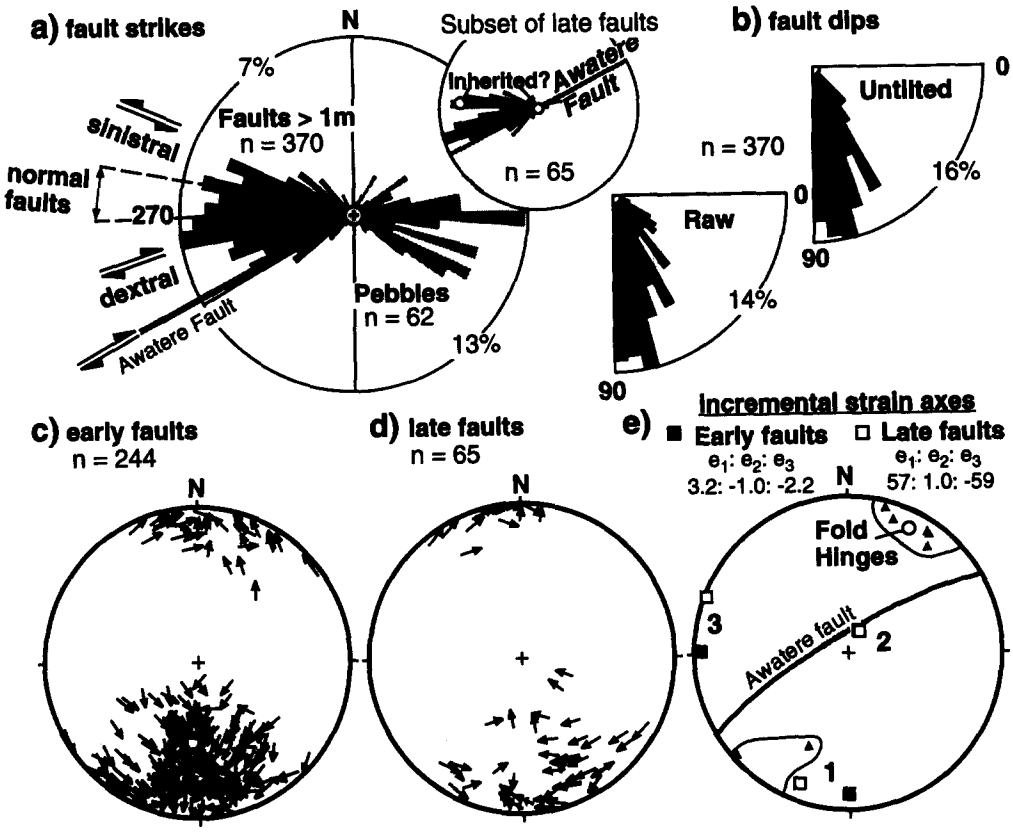

Fig. 5. Kinematic data for faults at White Bluffs. (a) Rose diagram of fault strikes (right-hand rule: dip direction is clockwise from strike); black cells refer to faults with lengths >1 m; grey-patterned cells refer to faults with lengths <1 m (bi-directional strikes); inset shows strike data for subset of late faults only. (b) Fault dips, uncorrected (on left) and with effect of stratal tilting undone (on right). (c) Slip-linears for early faults (pole to fault plane is represented by arrow showing sense of slip of footwall block; arrow is drawn tangent to movement plane of fault). (d) Slip-linear plot for late fault set. (e) Lower hemisphere stereogram showing hinges of folds in Neogene rocks (triangles). Numbers 1, 2 and 3 are greatest, intermediate and least principal strain directions calculated using Peacock & Sanderson (1993) method on (1) all early faults (closed boxes) and (2) all late faults (open boxes). Principal strain ratios are quoted relative to $e_2 = \pm$ unity.

from the Awatere fault and are sinistral. Several faults strike ~20° anticlockwise from the Awatere fault and are dextral (Fig. 5a, inset). A W-striking mode is interpreted to consist chiefly of oblique-normal faults that were inverted during the later transpressional deformation.

A stress inversion was not attempted on the late fault set because the subset with measured slip lineations is small. Figure 7 shows the relationship of fault-striation pitch to fault strike for dextral-reverse faults on which a slip-lineation was observed. These data were used to empirically assign a slip-vector pitch to faults lacking slip-lineations, based on their strike.

FAULT-SLIP MAGNITUDES

Calculation of finite displacement on faults

Fault-slip, offset, and location data were detailed in a compass-pace traverse of White Bluffs, with points on this traverse tied into a 1:25,000 scale topographic map. Differential weathering provided three-dimensional exposures of most faults; others were partially exhumed from the enclosing friable rock. Displacement vectors were calculated from input consisting of fault attitude, slip-lineation pitch, bedding attitude (determined from three–five apparent dip measurements), length and

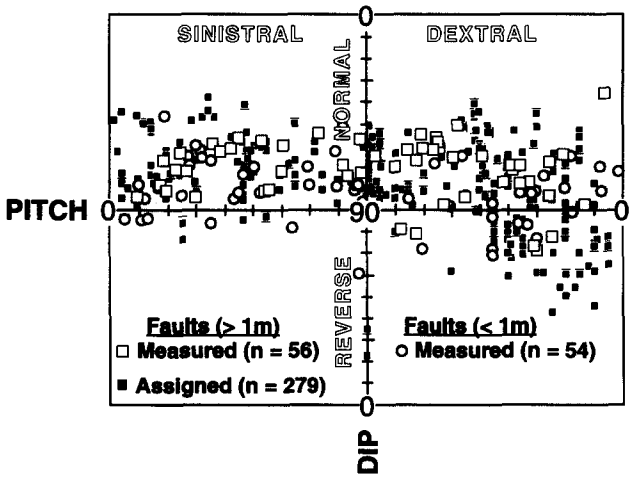

Fig. 6. Dip vs slip-vector pitch plot (after Angelier 1984). Open boxes—faults >1 m in length with measured slip-lineations; circles—pebble-length faults with measured net-slip vector; closed boxes—faults >1 m in length with assigned slip-vector pitches. Assignment of pitch was based on observed relationship between slip-vector pitch and fault strike (Fig. 7). See text for further discussion.

sense of bedding offset, and outcrop attitude (Fig. 8). In practice, a computer program used linear algebra to construct traces on the fault plane and then solved trigonometrically for the length and slip-sense of the net-slip vector, which was assumed to be parallel to fault slip-lineations. The calculations involved: (1) projecting bedding and outcrop surfaces onto the fault plane by calculating the vector cross-product of their poles with pole to the fault plane. This operation yields a trace on the fault plane for each surface. These traces are specified by their pitch angle relative to the fault's (right-hand rule) strike, as is the fault's slip-lineation; (2) the computer program logically compares the relative magnitude of these pitches and considers the sense of bedding separation on the outcrop before (3) using the law of sines to solve for the slip-vector magnitude, based on the outcrop-parallel bedding separation and the previously calculated angles between the traces. These define one leg and the vertices of a triangle on the fault plane. Slip-lineations were measured on 18% of the faults, either from wear grooves or from the net-slip of microfaulted conglomerate pebbles on or near the fault plane. For the rest, a slip-vector pitch was assigned to the fault, as described above. Stratal offset was uncertain on 10% of the faults, including the 14 largest. For these, a displacement magnitude was estimated using gouge thickness–displacement scaling relationships determined empirically from faults with known displacements. Two distinct styles of gouge were recognized on the basis of colour, texture, and microstructural characteristics, for which scaling ratios of 54 ± 30 and 1030 ± 600 were determined empirically by linear regression of data from faults at White Bluffs that have well-constrained displacements (R = 0.83 and 0.80, respectively) (Little in press).

Figure 5(e) plots the inferred principal directions of strain accomplished by all the early faults at White Bluffs, determined using the technique of Peacock & Sanderson (1993). This strain calculation technique assumes infinitesimal strain. Each fault is weighted according to (1) its displacement and (2) an inferred volumetric 'under-sampling' factor, dependent on its obliquity to the transect line. The analysis is conceptually equivalent to redistributing all the faults evenly across the sampled length of cliffs before obtaining a bulk strain. For the early fault set, the principal shortening direction trends W, the principal extension direction trends N, and the intermediate principal strain is sub-vertical (Fig. 5e). The relative magnitudes of these principal strains indicates a prolate shaped bulk strain ellipsoid. Application of the Peacock & Sanderson (1993) technique to the late fault set yields a principal shortening direction trending W–NW, a principal extension direction trending N–NE, and an intermediate principal strain that is sub-vertical (Fig. 5e). Note that axes related to the late faults are rotated about 20° clockwise with respect to the early fault set and suggest a slightly oblate strain ellipsoid.

Displacement–frequency scaling relationship

The result of the displacement calculations are compiled in Fig. 9, a log–log plot of locally observed displacement against cumulative number of faults having or exceeding that magnitude of displacement. The central part of the curve is linear, suggests a power-law scaling of fault slip over the range ~25–2000 cm, which is nearly two orders of magnitude. Interestingly, the fractal relationship appears to hold despite the data set being a combination of two kinematically distinct sets of faults. The lower curved tail in the data probably reflects under-sampling of the smallest faults, at least in part (faults with offsets of < 1 cm were not measured). The shape of this curve is similar to data presented by several other workers (Scholz & Cowie 1990, Marrett & Allmendinger 1991, Walsh & Watterson 1992, Peacock & Sanderson 1994).

Geographical distribution of fault displacement

The cliffs at White Bluffs may be divided into zones based on the style, spacing and intensity of post-early Pliocene faulting (Fig. 3). These are related to proximity to the Awatere fault and rock type. The active trace of the Awatere fault is concealed beneath a 9 m wide landslide (all widths refer to horizontal distances projected orthogonal to the strike of the Awatere fault). Outcrops farther inland reveal an ~50 cm thick gouge-filled core to the fault. In a traverse NW from the landslide, the first 53 m of outcrop at White Bluffs consists of densely faulted mudstone. In this damage zone, bedding has been tilted to dips of up to 52° and is complexly dismembered by a mesh of faults, spaced at ~1–30 cm.

Northwest of the damage zone, fault-bounded blocks of mudstone and lesser sandstone comprise zones 1 and 2 (Fig. 3). Laterally continuous turbidite markers in these blocks are cut and offset by faults, and can be traced from one block to the next in profile view.

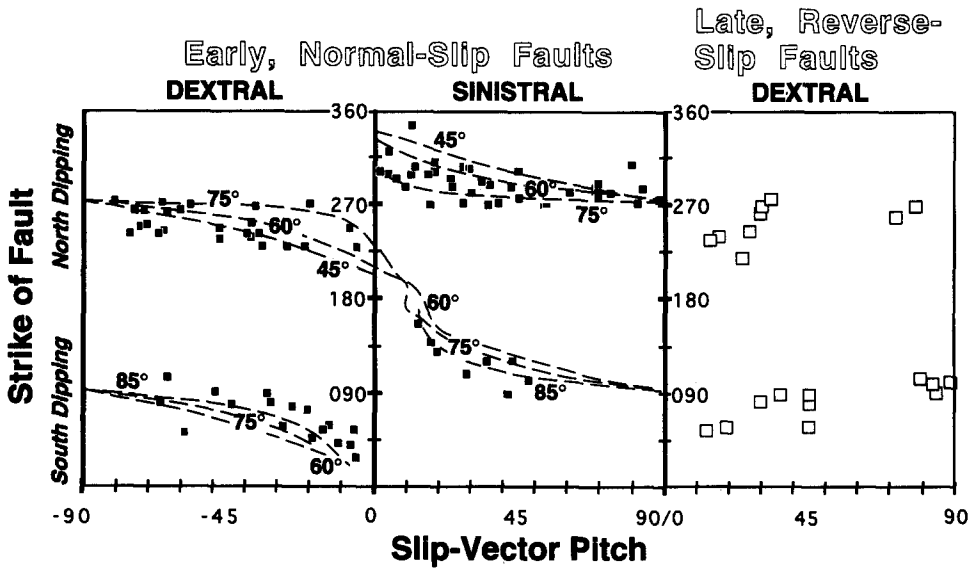

Fig. 7. Plot of fault strike against slip-vector pitch for subsets of faults with measured slip-lineations. Right-hand rule defines the strike as being anticlockwise from the dip direction. The left two columns contain data for early set of oblique-normal faults; the right column gives data for late set of dextral-reverse faults. Dashed curves for diferent fault dips were calculated by the technique of Ritz (1994), using best-fit results of a stress tensor inversion (Little in press).

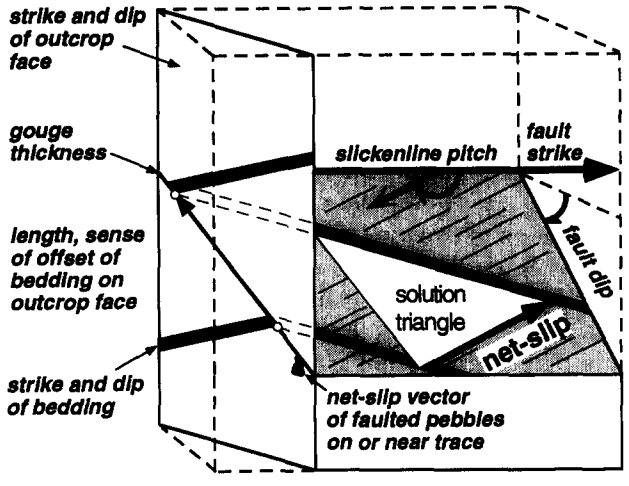

Fig. 8. Types of structural measurements made on White Bluffs transect. Italicized items are measured in the field. Computer program calculates net-slip vector for each fault based on input consisting of fault, bedding, and outcrop attitudes, slip-lineation pitch and sense and amount of bedding offset on the outcrop surface.

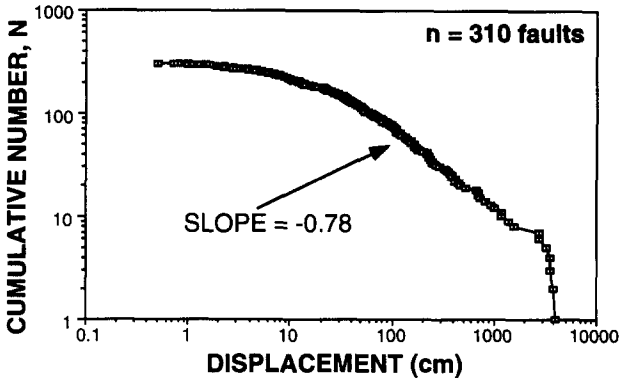

Fig. 9. Log–log plot of calculated fault displacement (in cm) vs cumulative number of faults, N, having or exceeding that magnitude of displacement. Note that this distribution refers to a linear sample of faults collected along a seacliff rather than a volumetric sample. The slope therefore corresponds to the scaling parameter C'_1 of Marrett & Allmendinger (1991). For 10% of the faults, including the 14 largest, a bedding offset was not observed on the outcrop plane, and displacements were inferred from empirical gouge thickness–displacement relationships (see text).

Colluvium and landslides obscure 54% of the 260 m length of zone 1. In 'the remaining' 121 m of composite outcrop, 114 faults were observed. As viewed parallel to the transect line, these are spaced on average ~1.1 m apart. Fifty of the faults are oblique-normal. The average observed displacement for normal-separation faults is about 1 m (range 0.01–14 m). Together, these faults contribute ~47 m of cumulative slip. Sixty-four of the faults are dextral-reverse. Most of these strike subparallel, or slightly clockwise from the Awatere fault. These have an average observed displacement of 4.8 m (range 0.01–37 m), and contribute a cumulative slip of ~297 m.

Zone 2 is 110 m wide. In a single, continuous outcrop 39 m long, 116 faults occur with a mean spacing of 0.3 m, as viewed along the transect plane. Of these 102 are oblique-normal faults. These have a mean observed displacement of 0.8 m (range 0.01–15 m), and contribute 80 m of cumulative slip. Dextral-reverse faults (n = 14) have a mean observed displacement of 1.2 m (range 0.02–10 m), and accrue 14 m of cumulative slip.

An ~750 m long stretch of inaccessible conglomeratic cliffs intervenes between zones 2 and 3. This change in lithology coincides with an abrupt increase of mean fault spacing (as observed along the transect line) to tens of metres. The mean observed dip separation (estimated from distant views of offset bedding) are about an order of magnitude greater. This suggests that the increased spacing between faults may be matched by a corresponding increase in slip. Thus displacement gradients in this domain may be similar to those in zone 2, however, no fault-slip data was collected in this zone to confirm this inference.

Zone 3, most distant from the Awatere fault, is 2.2 km wide, by far the largest and best exposed of the three zones. In 1.8 km of exposure, 93 faults, mostly oblique-normal, were observed in this zone. Although a few dextral-reverse faults are present, most of the faults dip > 80° south and would appear as normal-separation faults if stratal dip were removed. The zone consists chiefly of massive units of compact, clast-supported pebble–cobble conglomerate interbedded with subordinate mudstone–sandstone, in lenses from 0.4 to tens of metres thick. The mean fault spacing as viewed parallel to the transect is ~19 m, and the mean displacement, ~0.98 m (range 0.01–8.4 m).

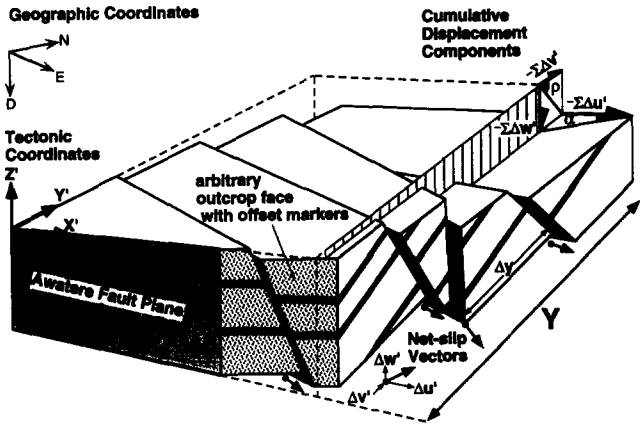

Fig. 10. Block diagram illustrating concept of displacement gradients in faulted rocks and meaning of notation used in text. Note that forward displacement vectors are shown, rather than the *reciprocal* displacements mentioned in text, but these differ only in their sign.

MEASUREMENT OF DISPLACEMENT GRADIENTS AND BULK STRAIN

Displacement summation technique

Several methods have been proposed to extract bulk strains from field data in faulted rocks (Molnar 1983, Krantz 1988, Jamison 1989, Wojtal 1989, Marrett & Allmendinger 1990, 1991, Cladouhos & Allmendinger 1993, Peacock & Sanderson 1993). All require excellent exposure, fault-slip information, and a representative sample of the regional fault population. In practice, these are formidable prerequisites. The technique of Krantz (1988) assumes irrotational deformation and simple orthorhombic fault geometries, thus limiting its applicability. Cladouhos & Allmendinger's (1993) method, although general, requires difficult to obtain information about the shape and dimensions of the sampled fault volume and is more complex. The moment tensor summation methods of Molnar (1983) and Marrett & Allmendinger (1990) also require volume estimation, as well as an assumption about the scaling relationship between net-slip and surface area of a fault. Peacock & Sanderson's (1993) modification avoids the above two pitfalls, permitting a bulk strain to be calculated from a linear sample of fault-slip data, but retains the assumption infinitesimal strain basic to all moment tensor summation techniques. All the above methods assume that a discontinuous displacement field associated with faulting can be approximated, at some scale, as a continuum deformation. This hypothesis can be tested (Wojtal 1986).

The method employed here (Fig. 10) is an adaptation of Wojtal's (1986, 1989) technique for fault strain measurement. Wojtal's original graphical method is practical where fault displacements are confined to a plane and where a well exposed array of faults offset distinct marker beds. Coordinate axes, $\mathbf{x}'$ and $\mathbf{y}'$, are inscribed into a deformed state cross-section that coincides with the movement plane. The section is graphically restored to its undeformed state by removing the displacement on each fault. The final and initial position of material points on the edges of each fault block are measured with respect to a *deformed* state coordinate system. The lengths

$$\Delta\mathbf{u}' = \mathbf{x} - \mathbf{x}' \quad (1a)$$

$$\Delta\mathbf{v}' = \mathbf{y} - \mathbf{y}' \quad (1b)$$

are defined as the *reciprocal* displacement components of the point $(\mathbf{x}', \mathbf{y}')$, and is the vector difference between positions in the undeformed and deformed states. These measurements are used to construct a *displacement diagram*, in which cumulative reciprocal displacements in the $\mathbf{x}'$ and $\mathbf{y}'$ directions, $\Sigma\,\Delta\mathbf{u}'$ and $\Sigma\,\Delta\mathbf{v}'$, are plotted as a function of distance along those two axes. For a two-dimensional case, four curves are obtained. These can be used to test the assumption that the displacement gradients are statistically homogeneous across a given domain. If the curves are approximately linear, their slopes correspond to the mean reciprocal displacement gradients, $\partial\mathbf{u}'/\partial\mathbf{x}'$, $\partial\mathbf{u}'/\partial\mathbf{y}'$, $\partial\mathbf{v}'/\partial\mathbf{u}'$, and $\partial\mathbf{v}'/\partial\mathbf{y}'$. These coefficients may be used to construct the reciprocal deformation gradient tensor, $\mathbf{D}^{-1}$, from which any of the bulk finite strain parameters may be calculated (Ramsay & Huber 1983). A further advantage of this simple technique is that the *locally* observed displacement on each fault is not used as an estimate of its *mean* displacement, something that the moment tensor summation techniques assume (Marrett & Allmendinger 1990).

Fault displacements need not be limited to a plane, but are three-dimensional. Thus reciprocal displacements in z are also considered,

$$\Delta\mathbf{w}' = \mathbf{z} - \mathbf{z}'. \quad (1c)$$

Displacement diagrams are computed algebraically from transect data using a computer spreadsheet program (Microsoft Excel). In theory, to specify all nine components of $\mathbf{D}^{-1}$ would require displacement data to be obtained from three mutually perpendicular transects, an unlikely possibility in the field. In practice, assumptions about the deformation field, such as constancy of volume, can reduce the number of independent variables. In a densely faulted zone adjacent to a major fault, one might assume that the zone's strike is a line of no finite elongation. This is equivalent to assuming that the rocks approximate a shear zone deforming by 'simple transpression' (Sanderson & Marchini 1984).

Simple transpression can be visualized as a combination of: (1) simple shearing parallel to the fault plane; (2) fault-normal extension or contraction of the fault zone. Volume is conserved in (2) by upward or downward displacement of the free surface. One way to test the above assumption is to compare strain results based on it with those derived from the same data set using a different technique not based on it, such as the Peacock & Sanderson (1993) method.

For convenience, all reciprocal displacement vectors were transformed from their geographic coordinates (East, North, Down) to a right-handed 'tectonic' coordinate system, in which $\mathbf{x}'$ is parallel to the strike of the Awatere fault (positive to the NE); $\mathbf{y}'$, horizontal; and $\mathbf{z}'$, vertically up (Fig. 10). Although the coordinate system could have been defined to coincide exactly with the 85° dipping Awatere fault plane, an upright coordinate system was chosen instead for ease of visualization. For oblique simple transpression in a zone parallel to the Awatere fault ($\mathbf{x}'$–$\mathbf{z}'$ plane), the reciprocal deformation gradient matrix is

$$\mathbf{D}^{-1} = \begin{bmatrix} 1 & \Gamma_{12} & 0 \\ 0 & k & 0 \\ 0 & \Gamma_{32} & k^{-1} \end{bmatrix} \quad (2)$$

where

$$\Gamma_{12} = \partial \mathbf{u}'/\partial \mathbf{y}' \text{ (effective strike-slip shear strain)} \quad (3)$$

$$k = 1 + \partial \mathbf{v}'/\partial \mathbf{y}' \text{ (zone-normal stretch)} \quad (4)$$

$$\Gamma_{32} = \partial \mathbf{w}'/\partial \mathbf{y}' \text{ (effective dip-slip shear strain)} \quad (5)$$

all refer to the *Eulerian* deformation process ('undoing' of the faults). Thus the three reciprocal displacement gradients in the $\mathbf{y}'$ direction completely specify the bulk deformation. Fault-displacement data from a single transect at right angles to the strike of the zone provide sufficient information to calculate a bulk finite strain. To do so, homogeneity of the displacement gradients in a given domain is first tested by inspection of the displacement diagrams. If the curves are approximately linear, coefficients (3), (4) and (5) may be determined by regression of the best-fit slopes and the matrix $\mathbf{D}^{-1}$ can be constructed. The reciprocal quadratic elongations, λ', and directions of the principal strain axes in the *undeformed* state can then be computed by finding the eigenvalues and eigenvectors of the Eulerian Finger tensor, $\mathbf{D}^{-1}(\mathbf{D}^{-1})^{\mathrm{T}}$. By factorizing $\mathbf{D}^{-1}$ into a left-stretch decomposition,

$$\mathbf{D}^{-1} = \mathbf{V}\cdot\mathbf{R} \quad (6)$$

the rotational component of deformation can be specified by reference to the orthogonal matrix, $\mathbf{R}$. From $\mathbf{R}$, the axis of rotation and rotation angle, α, may be calculated (Appendix A in Chen 1993). For a shear zone, this axis lies in the shear ($\mathbf{x}$–$\mathbf{z}$) plane. Applying the reverse rotation, $\mathbf{R}^{\mathrm{T}}$, to the previously determined principal strain axes determines their directions in the *deformed* state. Alternatively, $\mathbf{D}^{-1}$ may be inverted and the eigenvectors of the Lagrangian Finger tensor $\mathbf{D}\cdot(\mathbf{D})^{\mathrm{T}}$ computed to determine principal strain directions in the deformed state. Because we are trying to solve for a finite strain, the sequence of fault movements, in theory, must be specified (Wojtal 1989, Cladouhos & Allmendinger 1993). This consideration is important where faults are cross-cutting and have large displacements relative to their spacing. At White Bluffs, most faults are nearly vertical, intersections are uncommon, and displacement/spacing ratios are small.

Table 1. Summary of transect reciprocal displacement–length data used in strain calculations for each (sub)zone

Zone	Width, Y (m)	$\Sigma\Delta u'$ (m)	$\Sigma\Delta v'$ (m)	$\Sigma\Delta w'$ (m)
1a	66	−22.5	+1.5	−11.22
+1b	55	−259.1	−8.4	27.25
2	40	−11.2	+12.9	+2.59
3	1774	−32.2	−24.9	+23.61

Application to the White Bluffs fault array

Because of the complexity of faulting in the damage zone, the origin of the reference coordinate system is fixed on the southeast edge of zone 1, ~62 m from the trace of the Awatere fault. Fault-slip data were collected along a nonlinear series of legs following the arcuate seacliffs. The transect is thus not exactly parallel to the y direction. The distance increment between faults, Δy, was determined by projection of the measured leg distance onto the y coordinate direction (azimuth, 333), and displacement gradients in x are assumed to be negligible. Where breaks in exposure continuity occur, the transect position

$$y = \Sigma\Delta y \quad (7)$$

was kept fixed until the reappearance of outcrop. Thus the transect is a composite of data from available outcrops. These are assumed to provide a representative sampling of the faulting-related displacement field. Figure 3 summarizes the dimensions and amount of exposure for the several faulting zones.

Measured displacement gradients

Figure 11(a) presents the cumulative displacement data for fault-slip along the entire White Bluffs transect. In Fig. 12, these data are expanded to show details of the displacements gradients in each of the three zones. Faults were arbitrarily assigned to six types on the basis of their kinematics (Fig. 12).

In zone 1, adjacent to the Awatere fault, cumulative displacement components are non-linear, and suggest a division of zone 1 into two sub-zones, 1a and 1b, at about the point y = 65 m. Zone 1b has steep, transpressional displacement gradients controlled by slip on dextral-reverse faults striking sub-parallel to the Awatere fault. Displacements of 5–40 m are mostly inferred from gouge thickness data. These faults contribute > 300 m of dextral-slip across a zone width of only 120 m, and overwhelm smaller contributions by older oblique-normal faults.

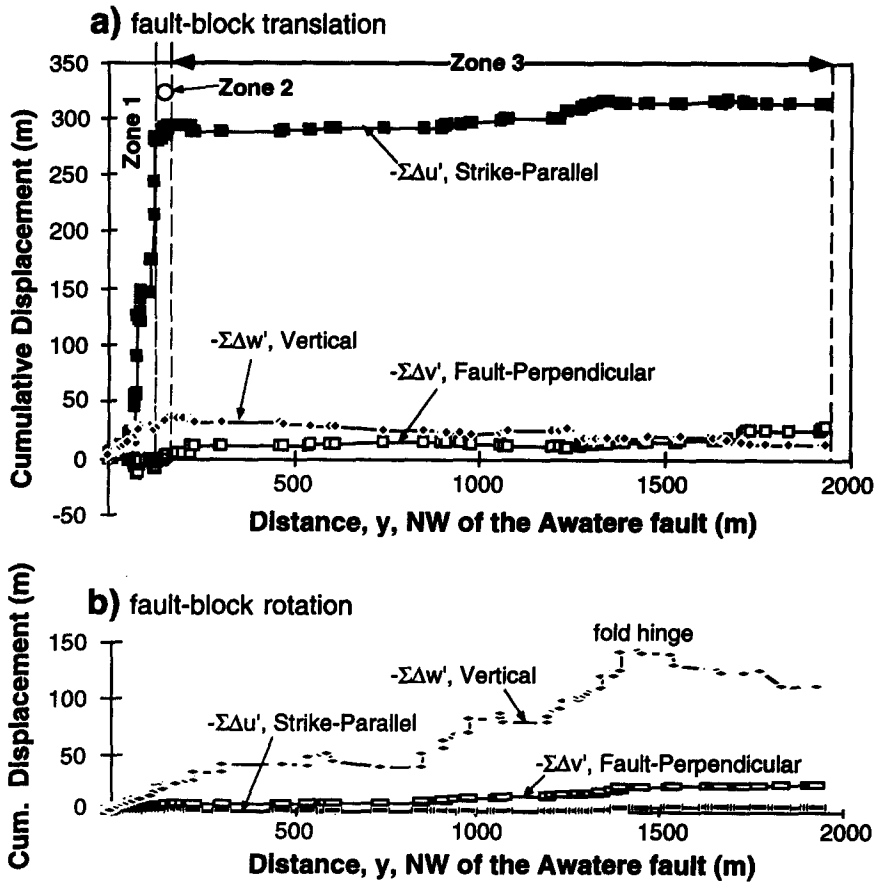

Fig. 11. Displacement gradients resulting from (a) fault-block translation and (b) fault-block rotation along White Bluffs transect. Displacement diagrams plot cumulative displacement in the three coordinate directions vs transect distance, y. In (b), the hump in the vertical ($-\Sigma\Delta w'$) component reflects competing effect of folding related to hinge of anticlinal fold in northern part of seacliffs at White Bluffs. Vertical exaggeration of both plots is 3:1. See text for further discussion.

Zone 2 consists chiefly of the early oblique-normal faults. Cumulative displacement curves are remarkably linear at length scales of 5–10 m, indicating nearly homogeneous bulk strain. In contrast to zone 1b, displacement gradients are gentle, the dominant sense of throw is down to the north, antithetic to the Awatere fault, and the fault-perpendicular component indicates net widening (transtension) of the deformation zone. Faults accrue < 20 m of dextral-slip across a distance of ~40 m. Half of this is accomplished on three large late-stage faults that disrupt the otherwise more linear curve for the strike-slip ($\Sigma\Delta u'$) component.

The pattern in zone 3 is similar to that in zone 2, but is accomplished by more widely spaced oblique-normal faults distributed across ~2 km of cliffs. Although punctuated by 'large' faults, the cumulative displacement gradient curves are nearly linear at length scales of ~100 m. Only 35 m of dextral-slip is accomplished across the ~2 km wide zone and all three cumulative displacement curves have quite gentle slopes indicating a bulk strain that is very small in magnitude.

Calculations of faulting-related strain

The displacement diagrams (Fig. 12) reveal that bulk displacement gradients in zones 2 and 3 are approximately homogeneous at length scales comparable to the width of the zones. Although the gradients in zone 1 are not homogeneous, division of the domain into two subzones allows the fault-slip data for each to be approximated by linear curves. Table 1 presents the measured widths (y) and cumulative reciprocal displacements for each part of the transect. Using the method and assumptions outlined in the previous section, these data were used to calculate bulk finite strains for each zone on the horizontal plane and in three dimensions (Table 2 and Fig. 13).

The results document a progressive reduction in strain intensity, as well as a change in kinematic style from transpressional to transtensional, with increased distance away from the Awatere fault (Fig. 14). In zone 1, the Y (intermediate) direction of finite strain is sub-vertical, lies near the plane of the Awatere fault, and pitches steeply north. Fault-perpendicular shortening and an oblate strain ellipsoid ($e_2 > 0$) indicate net transpression acting across both zones 1a and b. The X direction in these zones trends NE–SW, 45–30° anticlockwise from the strike of the Awatere fault, and reflects increasing transpressional strain going from zone 1a into zone 1b. Strain magnitudes are large, especially in zone 1b, which has an X/Z ratio of > 20 resulting from that zone's concentration of late dextral-reverse faults.

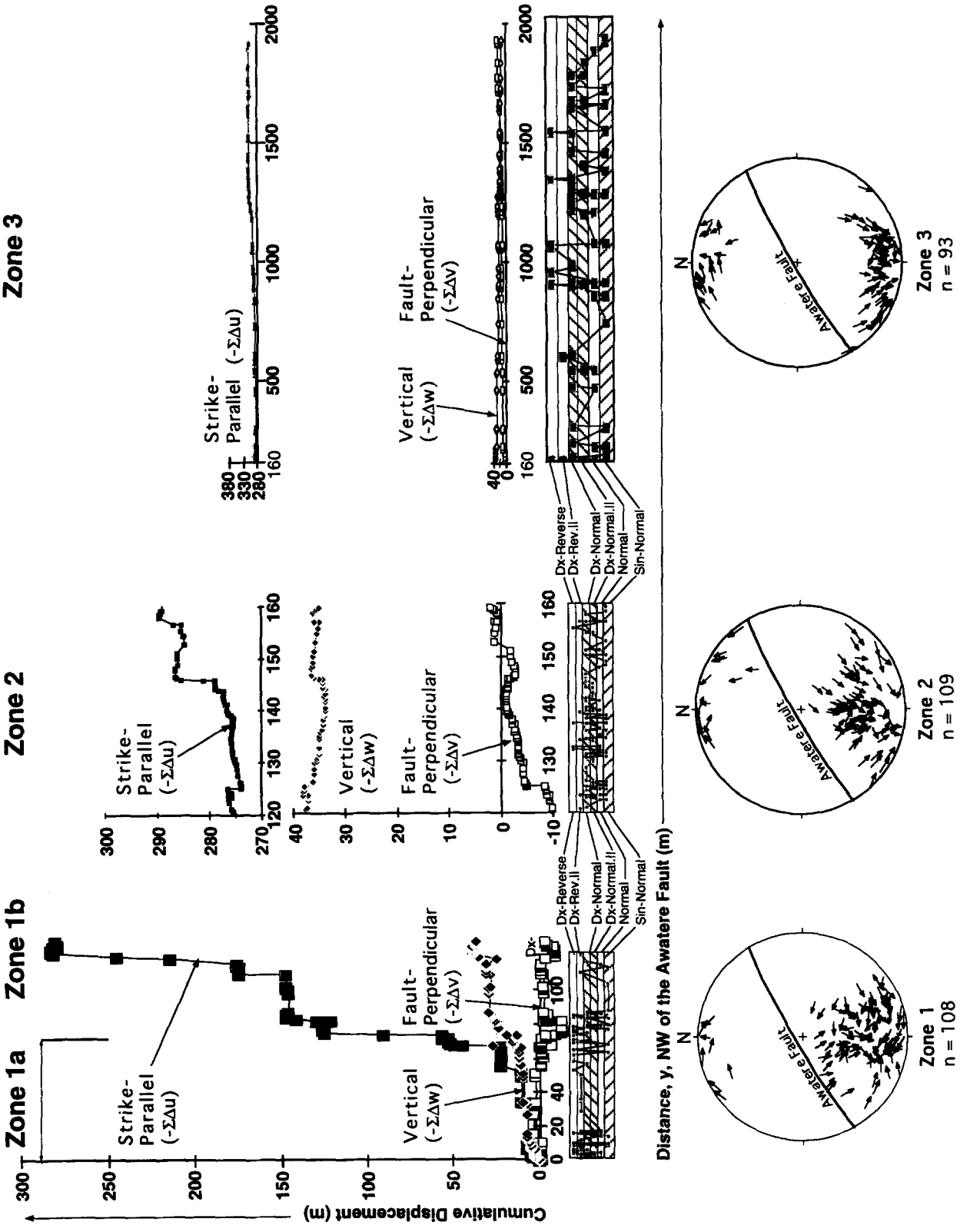

Fig. 12. Cumulative fault-slip displacement data for White Bluffs transect. Data is divided from left to right, into columns corresponding to the three main faulting zones (1, 2 and 3). Displacement diagrams in the centre of each column are expanded view of data plotted in Fig. 11. Because of differences in fault density, each zone is plotted at a different scale. No vertical exaggeration. Below the displacement diagrams are transect logs of fault kinematic type. The suffix (.|.) means a fault strikes within 13° of the Awatere fault. At base of each column is a stereographic projection showing slip-linear data for that zone, plotted as in Fig. 5(c).

Table 2. Finite strain results in two and three dimensions for White Bluffs. For zones 2 and 3, results from both the moment sum and displacement gradient techniques on the White Bluffs data set are presented. Asterisk for e_2 magnitude indicates positive sign (extension)

Zone	(Tr,pl) X	(Tr,pl) Y	(Tr,pl) Z	(+ve) e_1	(−ve) e_2	(−ve) e_3	X/Z Strain ratio	Rotation (°)	Dilatation $1 + \Delta A$	(Tr,pl) Rot. axis
			Two-dimensional calculations							
Zone 1a	192		112	0.17		0.16	1.4	10	0.98	vert.
Zone 1b	229		139	3.29		0.8	21.2	65	0.87	vert.
Zone 2	175		85	0.6		0.06	1.71	10	1.5	vert.
Zone 3	176		86	0.02		0.004	1.02	1	1.01	vert.
Moment summation technique										
Zone 2	179		089	0.67		0.15	1.96		1.67	vert.
Zone 3	180		090	0.02		0.01	1.03		1.01	vert.
			Three-dimensional calculations							
Zone 1a	199,24	054,63	295,14	0.197	0.018*	0.179	1.46	11	1.000	060,63
Zone 1b	230,10	033,79	139,03	3.339	0.151*	0.799	21.6	67	0.999	060,79
Zone 2	355,03	265,02	146,86	0.604	0.062	0.335	2.41	10	1.001	240,77
Zone 3	356,11	263,13	123,73	0.020	0.004	0.016	1.04	1	1.000	240,52
Moment summation technique										
Zone 2	179,17	333,72	087,8	0.183	0.065	0.117	1.34	6	0.977	338,61
Zone 3	004,8	114,69	271,20	0.025	0.009	0.015	1.04	1	1.001	290,62

In zones 2 and 3, Z is sub-vertical and nearly co-planar with the Awatere fault plane, rather than Y. Fault-perpendicular extension, a prolate strain ellipsoid ($e_2 < 0$), and a N-trending X direction ~60° anticlockwise from the strike of the Awatere fault, all reflect the transtensive kinematics of this part of the Awatere fault zone. Strain magnitudes are relatively large in zone 2 ($X/Z = 2.41$), but small in zones 3 ($X/Z = 1.04$). The vorticity (rotation of principal strain axes) is dextral and acts about a steeply plunging axis. It amounts to 65° in zone 1b, 10° in zones 1a and 2, and 1° in zone 3. This rotation is not expected to correspond to *fault-block* rotations observed in palaeomagnetic studies.

As a comparison of methods, and also a potential check on the simple transpression assumption, I used the same fault-slip data to calculate strains for zones 2 and 3 using the moment summation method of Peacock & Sanderson (1993) (Table 2). A comparison was not done for zone 1, as it clearly violates the infinitesimal strain assumption. By matrix transformation, the three-dimensional results of their method were also resolved onto the horizontal plane. For both techniques, the direction (X) of the greatest principal strain in zones 2 and 3, in both two and three dimensions, are comparable, and the other strain directions are also subparallel. Using either method, the calculated strain ellipsoid is prolate, and the strain magnitudes and rotations (vorticities) are similar. As expected, results of the two techniques are closest to one another for zone 3, where the infinitesimal strain assumption is justified. They differ, however, in that the sub-vertical principal strain axis for zones 2 and 3 computed by Peacock & Sanderson's (1993) moment summation technique is Y, not Z. Thus different assumptions used by the two methods for the same data set result in a 'swapping' of Y and Z in this case of prolate strain. The smaller magnitude of vertical strain determined by the displacement gradient technique may be a result of the simple transpression assumption, which assigns a vertical stretch, k^{-1}, based on conservation of volume, see equation (2).

DISCUSSION AND INTERPRETATION

Utility of Wojtal's (1986) technique for analysis of faulting in three dimensions

The results reported here indicate that this extension of Wojtal's (1986) strain measurement technique to three dimensions can be a useful tool for structural geologists analysing field data in faulted terranes. The method is practical only where the necessary trigonometric and matrix operations are calculated by microcomputer. Spreadsheet programs are well suited to this task because of their ease in entering repeated observations, and in searching, manipulating and graphing selected elements of large data sets. Simple matrix operations, such as rotation of field data or untilting of bedding, may also be performed for each site. Spreadsheet programs can also be used to model varying certain input parameters on the resultant finite strain. The method does not require assumptions about infinitesimal strain, fault volumes, fractal fault populations, or mean displacements on a fault. It is limited, however, by the one-dimensionality of most well-exposed fault population samples. Practical application of the method thus requires assumptions to be made about displacement vector field that may not be valid or are difficult to test. Even where only three reciprocal displacement components can be obtained, however, the method provides a powerful test of statistical homogeneity of the bulk faulting-related deformation, as well as useful and quantitative kinematic information.

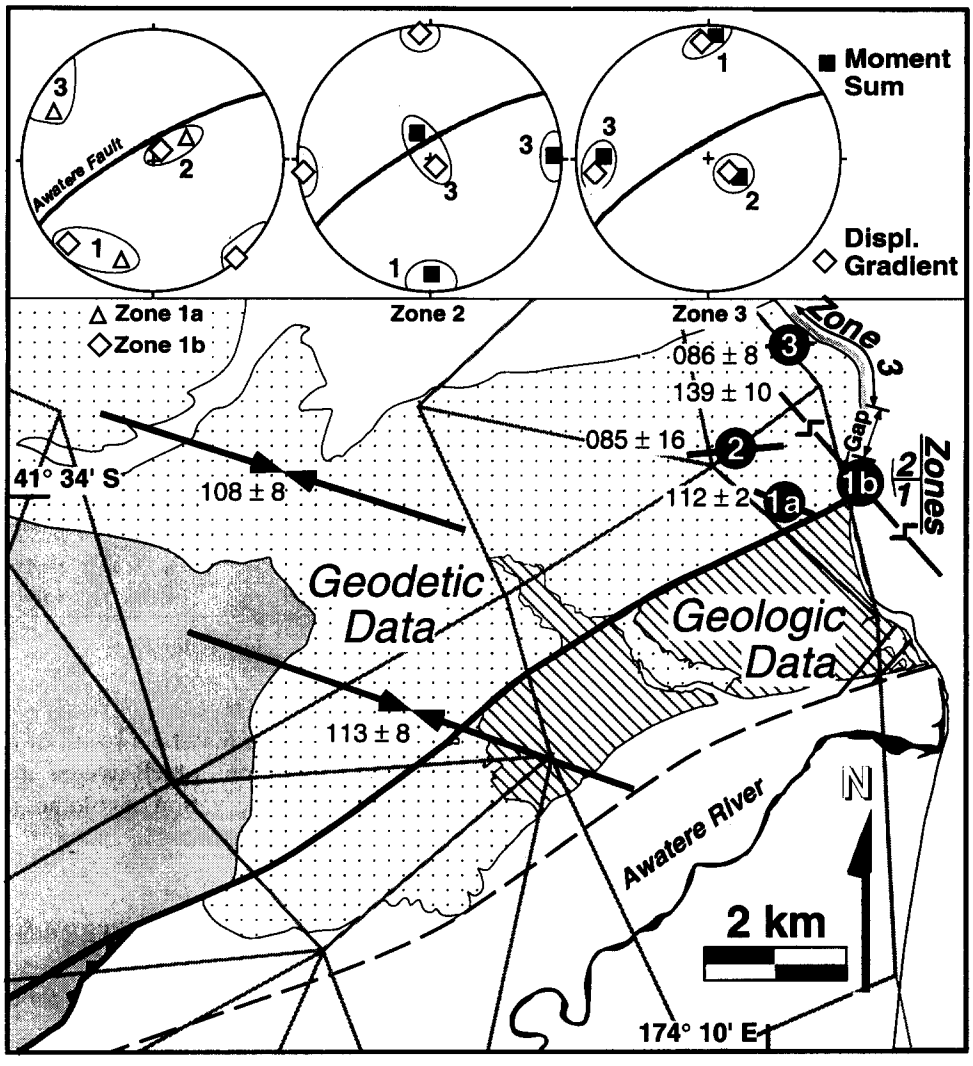

Fig. 13. Map showing comparison of geodetic strains with finite (or bulk) strains due to faulting in seacliffs at White Bluffs. Double arrows and numbers give azimuths of maximum horizontal principal shortening strain inferred geodetically from triangulation network employed by Bibby (1976, 1981); the coastal portion of this network is shown in grey lines. Ball-and-bar symbol and numbers show principal strain azimuths calculated from fault offsets in seacliffs at White Bluffs for zones 1a, 1b, 2 and 3. Length of azimuth symbols are proportional to maximum shear strain rate ($\times 10^{-6}\,yr^{-1}$). Maximum shear strain rates calculated for zones 3 and 1b in the cliffs are too small and large, respectively, to be shown to scale. Stereograms at top are lower hemisphere plots of principal strain orientations calculated for each zone at White Bluffs. Meaning of numbers 1, 2 and 3 are the same as in Fig. 5(e). Rates of finite longitudinal stretching cannot be directly compared with geodetic data since the triangulation network lacks a length scale. See text for discussion of assumptions and pitfalls in computation of these from finite strain data.

Comparison of finite and geodetic strain data near the Awatere fault

Bibby (1976, 1981) computed crustal strain rates across the eastern part of the Marlborough faults using repeated triangulation survey data based on initial surveys dating back to 1878–1884. Figure 13 shows the part of his geodetic network that overlaps with the White Bluffs region and illustrates its ~5 km length scale. Bibby derived two-dimensional strain results for: (1) the region between the Wairau and Awatere faults (this region is chiefly north of White Bluffs); (2) the area straddling the Awatere fault (this region includes most of White Bluffs). His results are presented in Table 3 and Fig. 13. Because repeated triangulation data consists of changes in angles without a length scale, only shear strain-rates, such as $\dot{\gamma}_{12}$ (rate of dextral shear), and azimuths of the principal strain axes can be specified from that data. If one assumes that the strike of the Awatere fault remains unchanged in length ('simple transpression'), then the geodetically measured shear strain-rates can be used to infer rates of shortening perpendicular to the fault ($\dot{e}_{22}$). The ratio of the dextral shear strain-rate/shortening rate, $\dot{\gamma}_{12}/\dot{e}_{22}$ measures the obliquity of the cumulative displacement vector relative to the strike of the Awatere fault (equivalent to angle α in Fig. 10).

To compare finite strains determined from fault-slip data in 5 m.y. old rocks with strain-rates measured geodetically during the past 100 yr requires two basic assumptions: (1) that finite deformation has accumulated at a steady rate (and incremental orientation) since inception of the Marlborough faults; (2) that this inception age is known. Plate reconstructions for the

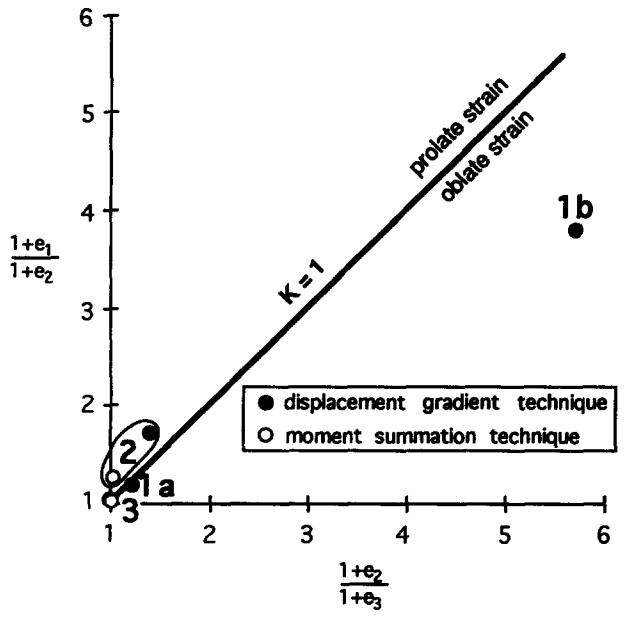

Fig. 14. Flinn plot showing shape of three-dimensional strain ellipsoids determined from transect fault-slip data for different zones adjacent to the Awatere fault.

Australia–Pacific plate margin based on seafloor spreading and Geosat data near New Zealand indicate a slight change in the Euler vector between anomaly 3 time (~5 Ma) and the present day (Mayes *et al.* 1990, DeMets *et al.* 1990). This change could have caused up to a 20° increase in the angle of relative convergence of the Pacific plate during that period. Thus the first assumption may not be valid. Euler vectors for stages prior to anomaly 3 are not yet available for this margin, however, and would not provide a measure of *deformation* rate at any site. I assume an inception age for the faults of ~5 m.y., the age of foraminifera in the upper part of the faulted cliff section (earliest Pliocene, P. Vella personal communication 1995). An ~5 Ma age for the Marlborough faults agrees with the dominantly strike-slip style of deformation of early Pliocene rocks throughout Marlborough, the similar dip of late Miocene and early Pliocene strata where they occur together (Lamb & Bibby 1989), and the <7 m.y. old age of fault scarp-derived alluvial fan deposits in the central Awatere Valley (Little 1994). A fault inception age of <5 Ma cannot be ruled out, however.

Based on the above two assumptions, *finite* displacement data based on fault-slip observations (Table 1) were used to infer instantaneous strain *rates*. The rate of fault-orthogonal longitudinal extension, $\dot{e}_{22}$, was calculated by comparing the fault-perpendicular displacement, $\Sigma\Delta v$, with the zone's final width, y. Dividing the natural strain, $\ln(1 + e_{22})$, by the time elapsed ($t = 5$ Ma) yields a strain rate. To infer values of shear strain rate from the measured components of $\mathbf{D}^{-1}$ depends on the way in which that matrix is decomposed into increments of margin-parallel (trans-) and margin-orthogonal (-pression) deformation. Slightly different values of shear strain rate are derived from the finite displacement data depending on whether the total deformation is viewed as a simple shear followed by pure shear, or vice versa. To avoid this ambiguity, the simultaneous simple and pure shear matrix decomposition of Fossen & Tikoff (1993) was used to calculate a dextral shear strain rate ($\dot{\gamma}_{12}$). Table 3 presents strain rates for the several zones derived in this way from the fault-slip data, and compares them with Bibby's (1976, 1981) geodetic data for the same region.

In theory, uncertainties in the value of the calculated displacement gradients could be assessed by regression analysis of the error in the best-fit slope of the displacement diagrams. Such errors are small, however, in comparison to those caused by assigning slip-vector pitch to faults lacking slickenlines and by use of the empirical gouge thickness–displacement relation to calculate the total slip on some faults. To assess the effect of the latter on calculated strains, the spreadsheet was run repeatedly with slip-vector pitches on each fault of ±45° from those assigned in the preferred model (based on Fig. 7), and with a 10× range of gouge-displacement scaling ratios. This modelling suggests uncertainties of <50% for components of the reciprocal displacement gradient matrix in zones 1a, 2 and 3, and <100% in zone 1b, and were used to obtain the 'errors' reported in Table 3.

Comparison of the geodetic and faulting-related strain rates reveals: (1) that principal strain axes are not generally coincident between the two data sets; (2) that outside of zone 1, geodetic strains (over the past century) are uniformly transpressional; whereas the faulting-related strain rates are transtensive and smaller than the geodetic ones; and (3) that within zone 1, faulting-related strain rates are transpressional and larger than the geodetic ones. Geodetically measured axes of maximum shortening near and straddling the fault trend ~108 and ~113, respectively (Fig. 13) and are sub-parallel to those measured in adjacent regions of New Zealand (Fig. 1b). In contrast, the faulting-related finite strain axes in zones 2 and 3 trend 085, markedly anticlockwise from the geodetic azimuth. Only in zone 1, a narrow belt adjacent to the Awatere fault, are finite strain axes locally oriented sub-parallel to the geodetic ones. The geologically measured dextral shear strain rate parallel to the Awatere fault, γ_{12}, is more than an order of magnitude smaller in zone 3 (most of the transect) than that measured geodetically across the same area. In zone 2, the faulting-related shear strain rates are within a factor of 10 of the larger geodetic ones. In zone 1b, however, the fault-slip strain rates are more than 4× greater than the geodetic ones, reflecting a concentration of fault-slip within that narrow zone. Whereas geodetic deformation implies regional transpression throughout the survey network (e_{22} and α are negative), faulting in the transect chiefly accommodates an oblique extension (e_{22}, positive; α = 38–50°). Net transpression at White Bluffs is confined to zone 1. The relative magnitude (and sign) of the fault-normal strain rate component thus differs markedly between the two data sets.

The most obvious differences between the two data

Table 3. Calculations of two-dimensional strain rates on the horizontal plane. Comparison of results from geodetic data (Bibby 1976, 1981) and fault-slip data (see Fig. 13). Strain-rates calculated from finite strain data are based on two assumptions: (1) that deformation of early Pliocene–late Miocene sequence has accumulated at a steady rate; (2) that deformation began 5 Ma, after deposition of the youngest rocks. Data in parentheses consider the additional effect of fault-block tilting on the faulting-related bulk deformation. See text for further explanation

Data type	Zone	Dimension orthogonal to fault (m)	Maximum shortening azimuth	($\times 10^{-6}$ yr^{-1}) Maximum shear strain	($\times 10^{-6}$ yr^{-1}) γ_{12}	($\times 10^{-6}$ yr^{-1}) ε_{22}	α (degrees)
Geodetic	Awatere tilt zone	7000	113 ± 7	0.59 ± 0.14	0.14 ± 0.07	−0.16 ± 0.04	−30 ± 20
Geodetic	Wairau–Awatere	35000	108 ± 8	0.47 ± 0.12	0.12 ± 0.03	−0.05 ± 0.01	−12 ± 8
Fault-slip	Zone 1a	66	112(108) ± 2	0.07(0.09) ± 0.04	0.07(0.09) ± 0.03	−0.005(0.05) ± 0.003	−4(3) ± 3
Fault-slip	Zone 1b	55	139(139) ± 10	2.12(2.70) ± 97.9	0.88(1.11) ± 0.80	−0.03(−0.03) ± 0.02	−2(−2) ± 2
Fault-slip	Zone 2	40	085(085) ± 16	0.11(0.16) ± 0.96	0.07(0.09) ± 0.04	0.08(0.11) ± 0.03	49(51) ± 28
Fault-slip	Zone 3	1775	086(080) ± 12	0.005(0.008) ± 0.002	0.004(0.005) ± 0.002	0.003(0.006) ± 0.002	38(51) ± 23

sets are the orientation of the principal strain axes and the areal extent of the regions of transpressional deformation. These differences do not change if the fault is assigned a younger inception age, whereas absolute magnitudes of the strain-rate components will change, and are therefore less reliably compared. This exercise leads to the following conclusions: (1) most of the faults exposed at White Bluffs are relict from an earlier phase of oblique-normal faulting that was distributed across the entire 3 km extent of White Bluffs; (2) most of the ongoing deformation is not accommodated by distributed faulting, but is released during earthquake slip on dextral-reverse faults along or near the gouge-filled core of the Awatere fault. The geodetic strain is elastic.

The change in faulting style with time may have been caused by episodic changes in local fault-block kinematics or partitioning of slip between strands of the Marlborough faults. Another possible explanation for the transition in faulting style is the change in Australia–Pacific plate motions which occurred between 5 Ma and the present day. If a change in plate motion occurred at ~2.5 Ma, and dextral-reverse faulting was initiated in response to this, then the fault-slip derived strain rates in Table 3 would be too small. These rates would nearly double in zone 1 (where they are already high), but not significantly altered in zones 2 and 3, where finite-slip on the older oblique-normal faults is dominant. If a partial inversion of the normal faults occurred at this time, it was not enough to change the finite sense of dip-separation on the older faults. The basic observation that transpressional finite-strain is narrowly focused, whereas the geodetic strain is regional, means that the main conclusions are probably valid.

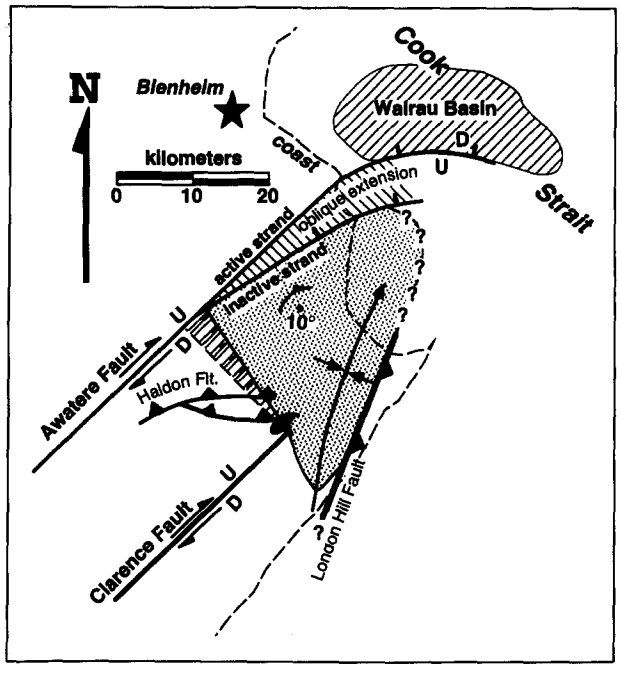

Fig. 15. Schematic fault block kinematic model of lower Awatere Valley region after Roberts (1995), based on palaeomagnetic data. The Awatere Valley fault block is pinned to seaward termination of Clarence fault. Distributed strike-slip shear drives rigid clockwise rotation of this block relative to rocks farther north. Dextral-oblique extension occurs in the Awatere fault zone along the northern boundary of the rotating block. Clockwise rotation may have resulted in slight misalignment of the southern strand of the Awatere fault, causing it to be replaced by the presently active strand. Offshore trace of Awatere fault and location of Wairau basin from Carter *et al.* (1988).

Faulting style in zones of oblique divergence (transtension)

Slip on the dominant, early set of oblique-normal faults accomplished a net transtension of the White Bluffs region. Using palaeomagnetic data, Roberts (1995) documented a 10° Neogene clockwise rotation of rocks southeast of the Awatere fault relative to rocks to the northwest, and inferred that the Awatere fault zone was located on a divergent boundary between two differentially rotating crustal fault blocks (Fig. 15). White Bluffs thus provides an excellent case study into the development of transtensive or divergent-wrench fault systems. Fault profiles at White Bluffs (e.g. Fig. 4) resemble the 'tulip-shaped', upward branching arrays of oblique-normal faults observed in seismic profiles of natural divergent wrench zones (Harding *et al.* 1985). Sanderson & Marchini (1984) and McCoss (1986) point out that a prolate finite and incremental strains, with X horizontal, are predicted for such zones, a feature which our strain analysis verifies for White Bluffs. The analysis of Reches (1983), which assumes irrotational deformation, predicts that this type of extensional triaxial bulk strain would, in theory, yield 4 sets of primary oblique-normal faults. While oblique-normal faulting is dominant at White Bluffs, rhomboidal fault sets like those described for coaxial deformation by Reches (1983) and Krantz (1988) are not present. Instead, if one ignores the complication of the late-stage faults, there is

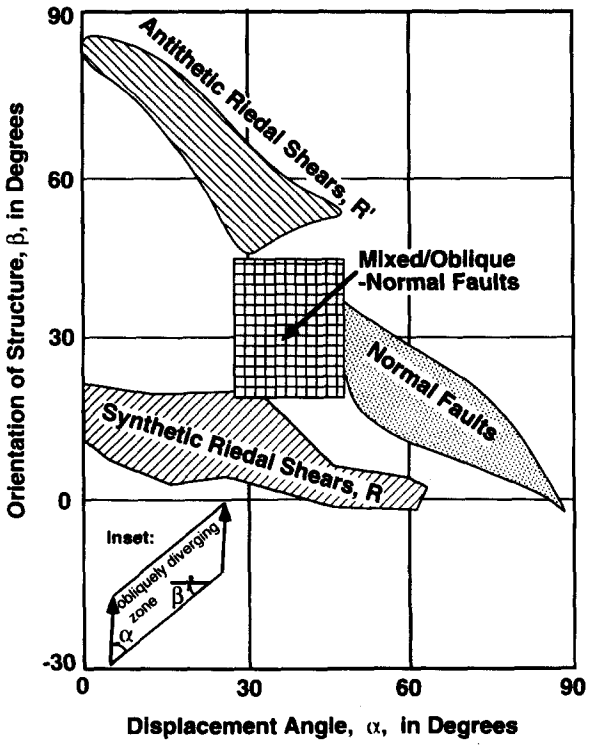

Fig. 16. Summary of fault kinematics derived from published experiments on obliquely diverging fault zones. Diagram plots strike of faults, given by angle, β, between fault strike and overall zone boundary, against the boundary displacement angle, α, for the zone (see inset). Hachured box shows region encompassing experimentally observed range of critical angles, α_{crit}, delimiting transition between conjugate strike-slip faulting and normal faulting. The early oblique-normal fault set at White Bluffs probably formed in the transition zone between these two 'Andersonian' regimes. Compiled from data in Smith & Durney (1992), Withjack & Jamison (1986), and Tron & Brun (1991).

a continuum of fault attitudes clustered about a N-dipping mode (Figs. 5a & c).

Experimental studies with clay and sand analogue materials using dextral-oblique displacement angles at α = 30–40° produce complex fault arrays dominated by moderately dipping oblique-normal faults similar to those found at White Bluffs. Most of the faults in the experiments (and at White Bluffs) strike ~30° clockwise from the strike of the rift margin (Naylor *et al.* 1986, Withjack & Jamison 1986, Tron & Brun 1991, Smith & Durney 1992). The oblique-normal faults bound tilted half-grabens that have a consistent dip direction. The mean fault dip decreases as the fault zone divergence angle, α, increases. For an angle of 40°, Tron & Brun (1991) observed a mean fault dip angle of ~65°, similar to that observed at White Bluffs. A subset of dextral-normal faults strike at a smaller angle (5–25°) clockwise from the rift margin. Less abundant faults, also oblique-normal, strike sub-parallel to, or bound, the rift margins and are dextral, or strike 40–60° clockwise from the rift margins and are sinistral. These studies predict a decrease in the conjugate (2θ) angle between dextral and sinistral strike-slip faults with increasing α (Fig. 16). Given the heterogeneity and scatter of natural fault populations, this decrease would blur the distinction between any 'conjugate' fault sets present and contribute to a unimodal fault pattern similar to the one seen at White Bluffs.

Experimentalists disagree on the 'critical displacement angle', α_{crit}, of opposite blocks in obliquely divergent rift zones above which distributed normal fault arrays will initiate in the zone rather than conjugate strike-slip faults. A useful feature of the displacement gradient analysis is that the net displacement angle, α, is measured from field data, not unlike in a laboratory experiment. In zones 2 and 3 at White Bluffs, rocks were transported at an angle of ~40–50° relative to the strike of the Awatere fault (angle α, in Fig. 10 and Table 3). This angle follows directly from the $\Sigma\Delta v'/\Sigma\Delta v'$ ratio of the cumulative displacement data. Recent theoretical and experimental studies observe a transition (or hybrid zone) between the two Andersonian faulting styles somewhere in the region α_{crit} = ~30–45° (Fig. 16). Differing estimates for the critical angle arise in part because of differing materials and boundary conditions used. In their clay model experiments, Withjack & Jamison (1986) observe a value of ~15–30°. Using elastic theory, they predict that the angle will vary with increasing Poisson's ratio from ~20°, where $\nu = 0.5$, to ~37° where $\nu = 0.25$, an analysis that agrees with the strain models of McCoss (1986) and Tikoff & Teyssier (1994). Both studies assume that the transition in faulting style occurs at the point where e_2 and e_3 of the instantaneous strain ellipsoid become equal and flip between horizontal and vertical. In contrast, Tron & Brun (1991) and Smith & Durney (1992) observe a α_{crit} of ~45° in their experiments, a transition that the latter attribute to a change in the sign of the vertical strain increment predicted by a dilatancy model of fault-deformation. In zones 2 and 3 at White Bluffs, which contain the early, oblique-normal fault set, α is ~40–50° and the fault population is dominated by dextral and sinistral oblique-normal faults, with subordinate normal dip-slip faults. The mixed or hybrid nature of this pattern supports the view that the actual value of α_{crit} for the rocks at White Bluffs is ~45°, rather than 20–30°.

Fault-block rotation is an important part of normal-fault related deformation, and thus contributes to displacement gradients. The effect of gentle folding on the tilt of gently dipping beds at White Bluffs is small in comparison with that of local fault block rotations, which cause a dispersion of poles about a mean E-trending, sub-horizontal axis (Fig. 2, inset, and Fig. 4). Figure 11(b) plots the cumulative displacement components resulting fault-block rotation at White Bluffs. Rotation is assumed to have occurred about bedding strike and to be equal in magnitude to the observed stratal dip. Displacement vectors were measured by pinning, in turn, the southern end of each block and rotating the adjacent transect point on the northern edge of the block to its pre-tilt position. These vectors were then summed sequentially across the length of the transect. The reciprocal deformation (retrodeformation) has thus been factorized into a fault-block translation (Figs. 11a and 12) followed by a rotation (Fig. 11b). The results illustrate that gentle stratal tilts causes

displacement chiefly in the vertical (z) and, to a lesser extent, fault-perpendicular (y) directions (Fig. 11b). The latter contributes to divergence or widening of the fault zone at White Bluffs. More importantly, it demonstrates that the magnitude of the rotation-related displacement gradients in this type of fault system are of about the same order as those caused by fault translation.

Nature of distributed faulting adjacent to a major strike-slip fault

The fault population at White Bluffs developed < 5 Ma at shallow crustal levels adjacent to a major strike-slip fault that is still active. Small-scale brittle faults in the hangingwall of the Awatere fault are densely spaced in a 300 m wide mudstone-rich zone adjacent to the fault, and widely spaced in a more distant, thick conglomerate unit. Fault arrays near the Awatere fault do not define a classic strike-slip (i.e. R–R'–P shear) pattern of polymodal strikes but are more gradationally distributed. Slip on these faults causes an increasing bulk finite strain with proximity to the trace of the active dextral-reverse fault. Geometric similarity of faults at different scales is supported by a consistent relationship between attitude and slip-vector pitch for faults with dip-parallel lengths of 10 cm to >250 m. The linear sample of faults defines a fractal scaling relationship between displacement (d) and cumulative frequency (ΣN) over approximately two magnitude orders in d (cm–m scale). The observed power-law exponent, C_1', for the linear transect is 0.78, where:

$$\Sigma N \sim d^{-C_1'} \tag{8}$$

(Marrett & Allmendinger 1991). Allowing the exponent, C_2, relating mean fault displacement to fault length:

$$d \sim l^{C_2} \tag{9}$$

(Marrett & Allmendinger 1991) to vary between 1.0 and 2.0, these data imply a volumetric displacement–frequency power-law exponent, C_1, of ~1.8–2.8 [Marrett & Allmendinger 1991, equations (4), (5) and (10)]. The power-law exponent, B, relating geometric moment (M_g) of faults to their cumulative frequency (ΣN):

$$\Sigma N \sim M_g^{-B} \tag{10}$$

obtained using equation 6(b) in Marrett & Allmendinger (1991) has a value of 0.89–0.93. A B value of 1.0 implies an equal contribution of strain by each magnitude range of faults, therefore small faults at White Bluffs provide an important but subordinate contribution to strain with respect to the largest faults in this complex fault zone (Marrett & Allmendinger 1990, 1991).

CONCLUSIONS

Extension of Wojtal's (1986) displacement gradient technique to three dimensions can be a powerful tool in the kinematic analysis of natural fault-slip data sets. The method is simple and avoids some assumptions used by other techniques of strain measurement in faulted rocks. To be useful in practice, the technique requires excellent exposure and a microcomputer to calculate and sum fault-slip vectors obtained from an input of outcrop measurements of offset. Enough slip-direction lineations must be observed on faults of differing attitudes to define a relationship between fault attitude and slip-vector pitch, which can be used to confidently assign a slip direction on faults lacking striations. In most cases, assumptions about the displacement field will be necessary in order to calculate a bulk finite strain from cumulative displacement data. In regions of active tectonic deformation, geodetically measured strain rates can, in principal, be compared with bulk finite-strains imprinted on young rocks by slip on observed arrays of macroscopic faults. Difficult-to-test assumptions will be necessary, however, in order to compare deformation rates over widely different length and time scales.

Slip on post-Pliocene faults near the dextral-reverse Awatere fault in New Zealand cause an increasing bulk finite strain with proximity to the trace of that active structure. Most faults are relict from an early phase of oblique-normal faulting accommodating an oblique divergence between differentially rotating crustal blocks. A younger set of dextral-reverse faults contribute a bulk kinematic pattern that is sympathetic with the sense of late Quaternary slip on the main structure. Like the earlier faults set, they are most densely spaced within 300 m of the Awatere fault.

Faulting-related finite strain axes are prolate (reflecting net transtension), except adjacent to the Awatere fault where they are oblate (reflecting transpression). These axes are generally not coincident with geodetic strain axes determined by triangulation across the same region during the past century. Dextral shear strain rates inferred from macroscopic fault-slip data are generally much smaller than the geodetic ones. Geodetic strain is transpressional over a large region, whereas the corresponding faulting-related deformation is transpressional only in the narrow zone along the fault. There, dextral-shear apparently accumulated at rates exceeding the regional geodetic ones. This pattern suggests that the ongoing deformation is not accommodated by distributed faulting, but is stored elastically and released during co-seismic slip along or near the trace of the Awatere fault.

The non-conjugate pattern of the early oblique-normal faults at White Bluffs probably developed in a zone of oblique divergence in a transitional state of stress between the two 'Andersonian' faulting regimes of normal and strike-slip faulting. Cumulative displacement data for the White Bluffs transect suggests that the net angle of divergence across the zone at the time of this faulting was ~40–50°. Fault-block rotation was subequal in importance to fault-slip in its contribution to the fault-perpendicular extension across the zone.

Geometric similarity of faults at different scales is

supported by slip kinematic data and by a fractal scaling relationship between displacement (d) and cumulative frequency (ΣN) over approximately two magnitude orders in d (cm–m scale). Small faults provide an important but subordinate contribution to strain relative to the largest faults.

Acknowledgements—This project was funded by New Zealand Foundation for Research, Science and Technology grant 94-VIC-30-907. Reviews by B. Tikoff and an anonymous reviewer, and editorial criticism by S. F. Wojtal, improved the paper. H. M. Bibby, R. I. Walcott, R. Marrett, and S. Thornley provided helpful advice on aspects of the study. R. W. Allmendinger provided a copy of the program Fault Kin 3.5, which was used to display some of the fault-slip data.

REFERENCES

Anderson, H., Webb, T. & Jackson, J. 1993. Focal mechanisms of large earthquakes in the South Island of New Zealand: implications for accommodation of Pacific–Australia plate motion. *Geophys. J. Int.* **115**, 1032–1054.

Angelier, J. 1984. Tectonic analysis of fault slip data sets. *J. geophys. Res.* **89**, 5835–5848.

Arabasz, W. J. & Robinson, R. 1976. Microseismicity and geologic structure of the northern South Island, New Zealand. *N.Z. Jl Geol. Geophys.* **19**, 569–601.

Bibby, H. M. 1976. Crustal strain across the Marlborough faults, New Zealand. *N.Z. Jl Geol. Geophys.* **19**, 407–425.

Bibby, H. M. 1981. Geodetically determined strain across the southern end of the Tonga–Kermadec–Hikurangi subduction zone. *Geophys. J. R. astr. Soc.* **66**, 513–533.

Carter, L., Lewis, K. B. & Davey, F. 1988. Faults in Cook Strait and their bearing on the structure of central New Zealand. *N.Z. Jl Geol. Geophys.* **31**, 431–446.

Chen, R. T. 1993. Strain factorization by identical finite increments and its use. *J. Struct. Geol.* **15**, 207–218.

Cladouhos, T. T. & Allmendinger, R. W. 1993. Finite strain and rotation from fault slip data. *J. Struct. Geol.* **15**, 771–784.

Cowan, H. A. 1990. Late Quaternary displacements on the Hope fault at Glynn Wye, North Canterbury. *N.Z. Jl Geol. Geophys.* **33**, 285–293.

Cowie, P. A. & Scholz, C. H. 1992. Displacement-length scaling relationship for faults: data synthesis and discussion. *J. Struct. Geol.* **14**, 1149–1156.

DeMets, C., Gordon, R. G., Argus, D. F. & Stein, S. 1990. Current plate motions. *Geophys. J. Int.* **101**, 425–478.

Fossen, H. & Tikoff, B. 1993. The deformation matrix for simultaneous simple shearing, pure shearing and volume change, and its implications to transpression–transtension tectonics. *J. Struct. Geol.* **15**, 413–422.

Gephart, J. W. 1990. FMSI: a FORTRAN program for inverting fault/slickenside and earthquake focal mechanism data to obtain the regional stress tensor. *Comput. Geosci.* **16**, 953–989.

Hancock, P. L. 1985. Brittle microtectonics—principles and practice. *J. Struct. Geol.* **7**, 437–457.

Harding, T. P. C., Vierbuchen, R. C. & Christie-Blick, N. 1985. Structural styles, plate tectonic settings, and hydrocarbon traps of divergent (transtensional) wrench faults. In: *Strike-Slip Deformation, Basin Formation and Sedimentation* (edited by Biddle, K. T. & Christie-Blick, N.). *Soc. Econ. Palaeont. Miner. Spec. Publ.* **37**, 51–77.

Jamison, W. R. 1989. Fault-fracture strain in Wingate Sandstone. *J. Struct. Geol.* **11**, 959–974.

Kneupfer, P. L. K. 1992. Temporal variations in latest Quaternary slip across the Australian–Pacific plate boundary, northeastern South Island, New Zealand. *Tectonics* **11**, 449–464.

Krantz, R. W. 1988. Multiple fault sets and three-dimensional strain: theory and application. *J. Struct. Geol.* **10**, 225–237.

Lamb, S. H. 1988. Tectonic rotations about vertical axes during the last 4 Ma in part of the New Zealand plate boundary zone. *J. Struct. Geol.* **10**, 875–893.

Lamb, S. H. & Bibby, H. 1989. The last 25 Ma of rotational deformation in part of the New Zealand plate boundary zone. *J. Struct. Geol.* **11**, 473–492.

Little, T. A. 1994. Late Cenozoic tectonics of the Awatere Fault, New Zealand (abstract). *Geol. Soc. N.Z. Misc. Publ.* **80A**, 117.

Little, T. A. In press. Brittle deformation adjacent to the Awatere strike-slip fault in New Zealand: faulting patterns, scaling relationships, and displacement partitioning. *Bull. geol. Soc. Am.*

Marrett, R. & Allmendinger, R. W. 1990. Kinematic analysis of fault-slip data. *J. Struct. Geol.* **12**, 973–986.

Marrett, R. & Allmendinger, R. W. 1991. Estimates of strain due brittle faulting: sampling of fault populations. *J. Struct. Geol.* **13**, 735–738.

Mayes, C. L., Lawver, L. A. & Sandwel, D. T. 1990. Tectonic history and new isochron chart of the South Pacific. *J. geophys. Res.* **95**, 8543–8567.

McCoss, A. M. 1986. Simple constructions for deformation in transpression/transtension zones. *J. Struct. Geol.* **8**, 715–718.

Molnar, P. 1983. Average regional strain due to slip on numerous faults of different orientations. *J. geophys. Res.* **88**, 6430–6432.

Naylor, M. A., Mandl, G. & Sijpeseijn, C. H. K. 1986. Fault geometries in basement induced wrench faulting under different initial stress states. *J. Struct. Geol.* **8**, 737–752.

Norris, R. J., Koons, P. O. & Cooper, A. F. 1990. The obliquely convergent plate boundary in the South Island of New Zealand: implications for ancient collision zones. *J. Struct. Geol.* **12**, 715–726.

Peacock, D. C. P. & Sanderson, D. J. 1993. Estimating strain from fault slip using a line sample. *J. Struct. Geol.* **15**, 1513–1516.

Peacock, D. C. P. & Sanderson, D. J. 1994. Strain and scaling of faults in the chalk at Flamborough Head, U.K. *J. Struct. Geol.* **16**, 97–107.

Pearson, C. 1993. Rate of co-seismic strain release in the northern South Island, New Zealand. *N.Z. Jl Geol. Geophys.* **36**, 161–166.

Pollard D. D., Saltzer, S. D. & Rubin, A. M. 1993. Stress inversion methods: are they based on faulty assumptions? *J. Struct. Geol.* **15**, 1045–1054.

Ramsay, J. G. & Huber, M. I. 1983. *The Techniques of Modern Structural Geology—Volume* 1: *Strain Analysis*. Academic Press, London.

Reches, Z. 1983. Faulting of rocks in three-dimensional strain fields II. Theoretical analysis. *Tectonophysics* **95**, 133–156.

Ritz, J.-F. 1994. Determining the slip vector by graphical construction: use of a simplified representation of the stress tensor. *J. Struct. Geol.* **16**, 737–742.

Roberts, A. 1995. Tectonic rotation about the termination of a major strike-slip fault, Marlborough fault system, New Zealand. *Geophys. Res. Lett.* **22**, 187–190.

Roberts, A. P. 1992. Palaeomagnetic constraints on the tectonic rotation of the southern Hikurangi margin, New Zealand. *N.Z. Jl Geol. Geophys.* **35**, 311–323.

Russel, W. A. C. 1959. A geological reconnaissance of northeast Marlborough. *N.Z. Geol. Surv. Petrol. Rep.* **279**.

Sanderson, D. J. & Marchini, R. D. 1984. Transpression. *J. Struct. Geol.* **6**, 449–458.

Scholz, C. H. & Cowie, P. A. 1990. Determination of total geologic strain from faulting. *Nature* **346**, 837–839.

Smith, J. V. & Durney, D. W. 1992. Experimental formation of brittle structural assemblages in oblique divergence. *Tectonophysics* **216**, 235–253.

Tchalenko, J. S. 1970. Similarities between shear zones of different magnitudes. *Bull. geol. Soc. Am.* **81**, 1625–1640.

Tikoff, B. & Teyssier, C. 1994. Strain modeling of displacement–field partitioning in transpressional orogens. *J. Struct. Geol.* **16**, 1575–1588.

Tron, V. & Brun, J.-P. 1991. Experiments on oblique rifting in brittle–ductile systems. *Tectonophysics* **188**, 71–84.

Van Dissen, R. & Yeats, R. S. 1991. Hope fault, Jordan thrust and uplift of the Seaward Kaikoura Range, New Zealand. *Geology* **19**, 393–396.

Walcott, R. I. 1978. Present tectonics and late Cenozoic evolution of New Zealand. *Geophys. J. R. astr. Soc.* **52**, 137–164.

Walcott, R. I. 1984. The kinematics of the plate boundary zone through New Zealand: a comparison of long and short term deformation. *Geophys. J.R. astr. Soc.* **79**, 613–633.

Walsh, J. J. & Watterson, J. 1992. Populations of faults and fault displacements and their effects on estimates of fault-related extension. *J. Struct. Geol.* **14**, 701–712.

Wellman, H. W. 1983. New Zealand horizontal kinematics. In: *Geodynamics of the Western Pacific–Indonesian Region* (edited by

Hilde, T. W. C. & Uyeda, S.). *Am. Geophys. Un. Geodyn. Ser.* **11**, 452–457.
Withjack, M. O. & Jamison, W. R. 1986. Deformation produced by oblique rifting. *Tectonophysics* **126**, 99–124.
Wojtal, S. 1986. Deformation within foreland thrust sheets by populations of minor faults. *J. Struct. Geol.* **8**, 341–360.
Wojtal, S. 1989. Measuring displacement gradients and strains in faulted rock. *J. Struct. Geol.* **11**, 669–678.
Wojtal, S. & Mitra, G. 1986. Strain hardening and strain softening in fault zones from foreland thrusts. *Bull. geol. Soc. Am.* **97**, 674–687.
Wojtal, S. & Pershing, J. 1991. Palaeostress associated with faults of large offset. *J. Struct. Geol.* **13**, 49–62.